Cell Reports

Article

Environmentally dependent and independent control of 3D cell shape

Graphical abstract

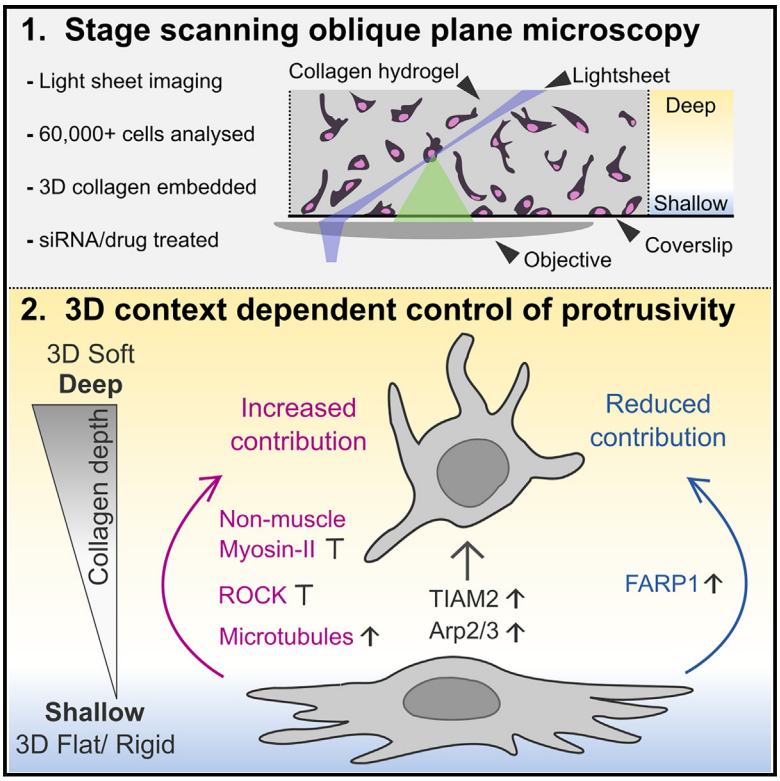

Highlights

- A 3D morphology analysis of more than 60,000 cells by high-throughput light sheet
- The environment modulates opposing roles of myosin and microtubules in shape control
- RhoGEFs *FARP1* and *TIAM2* control cell protrusivity in distinct environmental contexts
- A technique to assay cytoskeletal signaling in cancer cells in complex environments

Authors

Lucas G. Dent, Nathan Curry, Hugh Sparks, ..., Leo Rowe-Brown, Chris Dunsby, Chris Bakal

Correspondence

christopher.dunsby@imperial.ac.uk (C.D.), chris.bakal@icr.ac.uk (C.B.)

In brief

Using high-throughput light-sheet microscopy, Dent et al. study 3D cancer cell morphogenesis. Environmental cues modulate the opposing roles of non-muscle myosin II (myosin) and microtubules, with varied impacts on RhoGEFs *FARP1* and *TIAM2*. The study underscores the critical interplay between cytoskeletal regulators and the microenvironment, enhancing our understanding of cell behavior in diverse settings.

Dent et al., 2024, Cell Reports *43*, 114016
May 28, 2024
https://doi.org/10.1016/j.celrep.2024.114016

CellPress

Cell Reports

CellPress
OPEN ACCESS

Article

Environmentally dependent and independent control of 3D cell shape

Lucas G. Dent,[2,3] Nathan Curry,[1,3] Hugh Sparks,[1,4] Vicky Bousgouni,[2,4] Vincent Maioli,[1] Sunil Kumar,[1] Ian Munro,[1] Francesca Butera,[2] Ian Jones,[2] Mar Arias-Garcia,[2] Leo Rowe-Brown,[1] Chris Dunsby,[1,5,*] and Chris Bakal[2,5,6,*]

[1]Photonics Group, Department of Physics, Imperial College London, London SW7 2AZ, UK
[2]Dynamical Cell Systems Group, Division of Cancer Biology, Institute of Cancer Research, 237 Fulham Road, London SW3 6JB, UK
[3]These authors contributed equally
[4]These authors contributed equally
[5]These authors contributed equally
[6]Lead contact
*Correspondence: christopher.dunsby@imperial.ac.uk (C.D.), chris.bakal@icr.ac.uk (C.B.)
https://doi.org/10.1016/j.celrep.2024.114016

SUMMARY

How cancer cells determine their shape in response to three-dimensional (3D) geometric and mechanical cues is unclear. We develop an approach to quantify the 3D cell shape of over 60,000 melanoma cells in collagen hydrogels using high-throughput stage-scanning oblique plane microscopy (ssOPM). We identify stereotypic and environmentally dependent changes in shape and protrusivity depending on whether a cell is proximal to a flat and rigid surface or is embedded in a soft environment. Environmental sensitivity metrics calculated for small molecules and gene knockdowns identify interactions between the environment and cellular factors that are important for morphogenesis. We show that the Rho guanine nucleotide exchange factor (RhoGEF) *TIAM2* contributes to shape determination in environmentally independent ways but that non-muscle myosin II, microtubules, and the RhoGEF *FARP1* regulate shape in ways dependent on the microenvironment. Thus, changes in cancer cell shape in response to 3D geometric and mechanical cues are modulated in both an environmentally dependent and independent fashion.

INTRODUCTION

The ability of metastatic cancer cells to invade three-dimensional (3D) structures such as tissues and organs is dependent on cytoskeletal changes in response to factors such as stiffness and geometry.[1–6] Collagen is an abundant protein in human tissues, and collagen hydrogels are a common model to study cancer morphogenesis in 3D. In compliant 3D collagen environments, cells have been observed to adopt "mesenchymal" or "ameboid" shapes.[7–9] In contrast, cells tend toward the ameboid form in rigid low-adhesion[10–14] or highly confined environments.[2,3,15,16] Different collagen compositions can drive alterations in cell shape depending on properties such as elastic modulus, collagen cross-linking, and pore size.[17–20] Importantly, the ability of some cells to switch between mesenchymal and ameboid forms likely provides cancer cells with the ability to invade substrates with different stiffnesses and geometries.[7,21,22] However, there is little quantitative understanding of how cells couple shape determination to the forces and geometries of 3D environments and how this process may be dysregulated in cancer cells.

Changes in cytoskeletal, lipid, and adhesion organization that determine cell shape in response to the cell environment are regulated by Rho GTPase proteins such as RHOA, RAC1, and CDC42.[23,24] Canonically, RHOA activation is associated with increased activation of Rho-associated protein kinases (ROCKs), which upregulate myosin-II-mediated contractility at the cell cortex and cell rounding.[25,26] In contrast, RAC1 activation leads to increased WAVE activity, polymerization of branched actin structures, and protrusive structures such as lamellipodia.[27] CDC42 promotes the polymerization of filamentous actin structures, such as filopodia, and also promotes contractility through activation of PAK2 in some contexts.[23,24,28,29]

Additional layers of regulation by Rho guanine nucleotide exchange factors (RhoGEFs) and Rho GTPase activating proteins (RhoGAPs) couple the spatiotemporal dynamics of Rho GTPase activity to environmental flux.[30,31] RhoGEFs increase the signaling activity of GTPases by promoting the release of GDP and loading of GTP.[32] RhoGAPs decrease the activity of Rho GTPases by catalyzing hydrolysis of GTP to GDP.[33] RhoGEFs and RhoGAPs have been shown to confer environmental responsiveness through recruitment and activation of Rho GTPases at distinct subcellular locations. For example, ARHGEF7 and SRGAP1 play important roles in regulating cell shape in 3D collagen versus fibronectin gels.[34] Pioneering studies have shown that in melanoma cells, RhoGEFs, RhoGAPs, and Rho GTPases regulate the conversion between adhesion-based mesenchymal shapes and/or cortical tension-based ameboid and lobopodial forms.[7–9,11,35] Despite this, in many instances, the RhoGEFS/GAPs that allow cancer

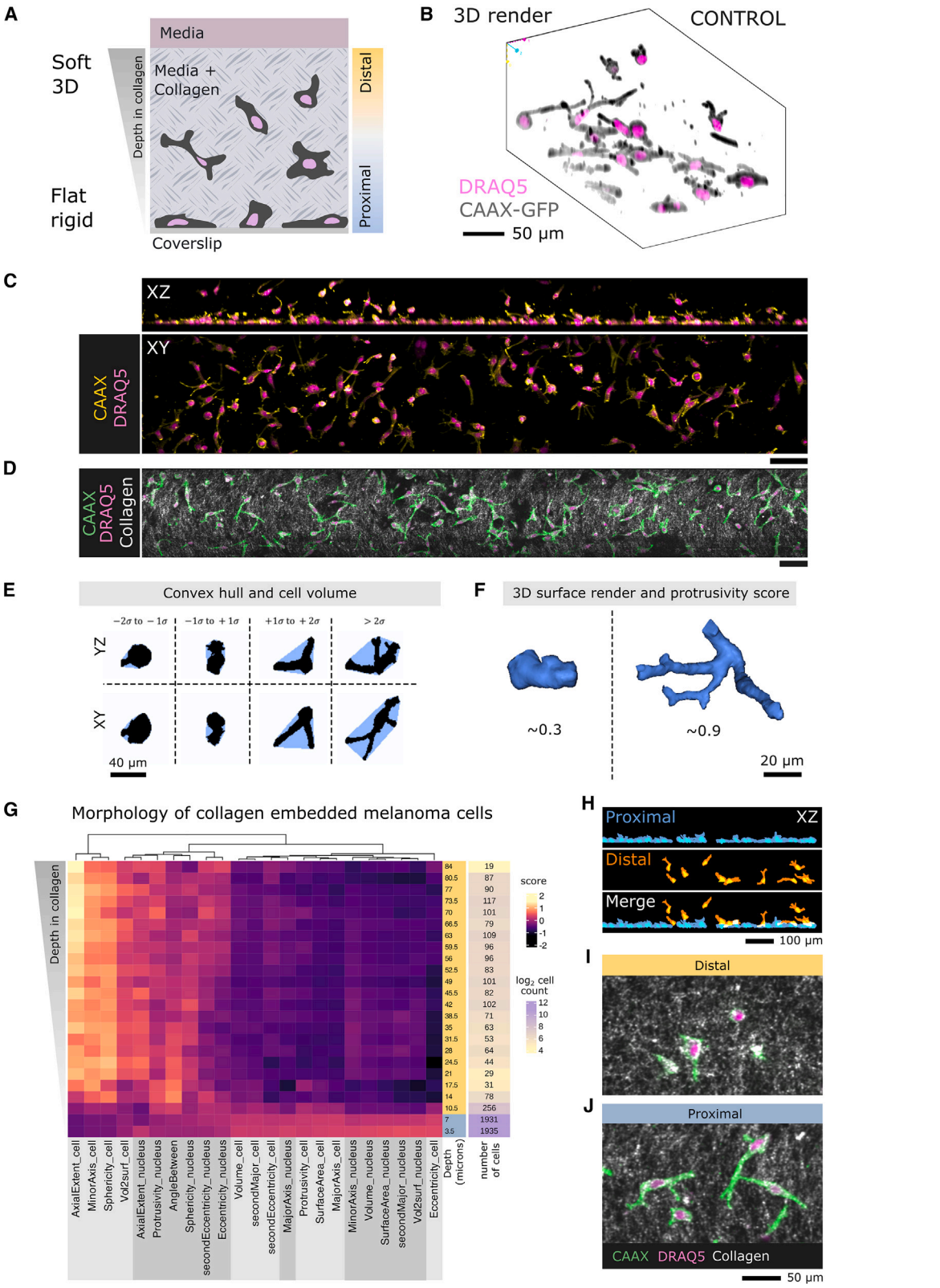

(legend on next page)

cells to respond to a particular environmental context remain to be identified.

To better understand the relationship between 3D environments and cell morphology, as well as to identify the genes and proteins important for coupling of environment to shape, we used stage-scanning oblique plane microscopy (ssOPM)[36] to perform 3D imaging of melanoma cells cultured in 3D collagen hydrogels. In this model, cells are either deeply embedded in the collagen hydrogel or adjacent to a rigid and flat surface (Figure 1A). This technique is based on oblique plane microscopy (OPM), where the same high NA objective delivers the light sheet and collects the fluorescence.[37] This system is built around a standard microscope frame and uses standard multiwell plates. We retain the advantages of working with a standard microscope frame but gain fast 3D imaging for hundreds of cells per minute.

To gain mechanistic insight into 3D shape determination of cancer cells in collagen hydrogels, we performed quantitative morphological profiling[39] of 3D cell shape. We did this in untreated cells, in cells exposed to small-molecule inhibitors of cytoskeleton organization, and cells treated for depletion of different Rho GTPase regulators. We identified stereotypic and environmentally dependent changes in shape and protrusivity depending on whether a cell is adhered to a flat and rigid surface or is embedded in a 3D soft environment. By calculating environmental sensitivity metrics for small molecules and gene knockdowns, we identified interactions between the environment and cellular factors that are important to shape determination. We show that the RhoGEF *TIAM2* contributes to shape determination in environmentally independent ways but that non-muscle myosin II (NMII), microtubules (MTs), and the RhoGEF *FARP1* regulate shape in ways dependent on the microenvironment, especially environmental geometry. Focusing on cell protrusivity, we found that depletion of the RhoGEF *TIAM2* diminished protrusivity and increased signs of NMII-dependent contractility in both flat/rigid and soft fully 3D environments. In contrast, depletion of the RhoGEF *FARP1* was only required for protrusivity in coverslip-proximal (flat/rigid) environments. These data demonstrate that signaling networks are capable of regulating morphology depending on a cell's local 3D environment. Taken together, these results reveal context-specific regulators of protrusivity and highlight the ability of high-throughput plate-based volumetric imaging to rapidly assay and identify genes and proteins in control of cell shape.

RESULTS

A 3D imaging assay to measure cell shape in distinct environments

To study 3D morphogenesis in mechanically and geometrically distinct environments, we developed a pipeline to quantify the shape of single melanoma cells in collagen hydrogels polymerized on either glass or cyclic olefin polymer (plastic). Glass and plastic are rigid substrates with a modulus of elasticity on the order of 60–64 and 1.25–5.49 GPa, respectively. In contrast, collagen is relatively elastic. Measurements of collagen stiffness vary due to differences in deformation mode and hydrogel preparation; however, stiffness generally increases with concentration.[19] Examples of stiffness measures for collagen concentrations between ~0.5 to 7 mg/mL range from ~60 Pa to more than 1,500 Pa.[40–43] Cells situated on softer substrates, such as collagen overlayed on a rigid base, are thought to respond to the properties of both the soft and rigid materials.[44–46] In our model, a subpopulation of collagen-embedded cells is adhered to or near the flat and rigid surface at the bottom of the hydrogel (Figures 1A and 1B). This allowed us to use ssOPM to simultaneously image the 3D geometry of cells adhered to flat surfaces and those embedded in the collagen hydrogel (Figures 1C and 1D). We used ssOPM to image CAAX-GFP-expressing WM266-4 cells with nuclei marked by DRAQ5 (STAR Methods) in collagen hydrogels on glass (collagen on glass). We inspected these hydrogels by measuring scattered light intensity and found relatively uniform intensity across a range of depths (Figure S1). We scanned volumes in 96-well-plate format, and typically, each single image volume contained ~150–200 cells, imaged over an ~144 μm z range. In this study, we also analyzed a dataset that we acquired similarly for De Vries et al.[38] These data were of collagen hydrogels on plastic (collagen on plastic), and histone-RFP was used as a nucleus marker in place of DRAQ5. In total, we imaged and analyzed more than 28,500 single cells in collagen on glass (Table S3) and also analyzed a further dataset of more than 37,000 single cells in collagen on plastic[38] (Table S4).

Defining a protrusivity metric

First, we sought to define the shape space explored by melanoma cells in different environments. Initially, we generated over 20 measures of cellular or nuclear shape features (Tables S1 and S2). As cell protrusion and protrusivity are drivers of migration[47,48] and invasion and metastasis,[47,49,50] we created

Figure 1. Three-dimensional oblique plane microscopy of melanoma cells in distinct physical contexts

Images are from a collagen on glass dataset, and heatmap is from a collagen on plastic dataset from De Vries et al.[38] (C), (D), (H), (I), and (J) depict different views or enlargements of the same control-treated ssOPM image volume.

(A) Schematic of cells in collagen hydrogel, proximal (blue) and distal (yellow) to the coverslip.

(B) Three-dimensional rendering of control cells. Membranes are CAAX-GFP (inverted gray scale), and nuclei are DRAQ5 (magenta).

(C) Orthogonal maximum-intensity projection (MIP) subvolumes (xy and xz views) from a control well. CAAX-GFP, yellow; nucleus, magenta.

(D) xy subvolume section of control cells. CAAX-GFP, green; nucleus, magenta; collagen, gray.

(E) Two-dimensional projections of cell segmentation masks (black) and convex hull (blue) over indicated protrusivity ranges (σ is standard deviation).

(F) Examples of 3D renderings and protrusivity metric.

(G) Heatmap of shape feature *Z* scores for untreated cells from three experiments, 15 replicates. Cell count (right); color scale (purple-yellow) is $\log_2$ cell count.

(H) Segmentation masks from 3D collagen on glass; proximal (blue) and distal (orange) cells.

(I and J) xy views of cells in 3D collagen in proximal (blue) and distal (yellow) settings. The scale bar for (I) and (J) is shared. (J) is a zoomed region from (D). Scale bars: (B, I, and J) 50 μm, (C, D, and H) 100 μm, (E) 40 μm, and (F) 20 μm.

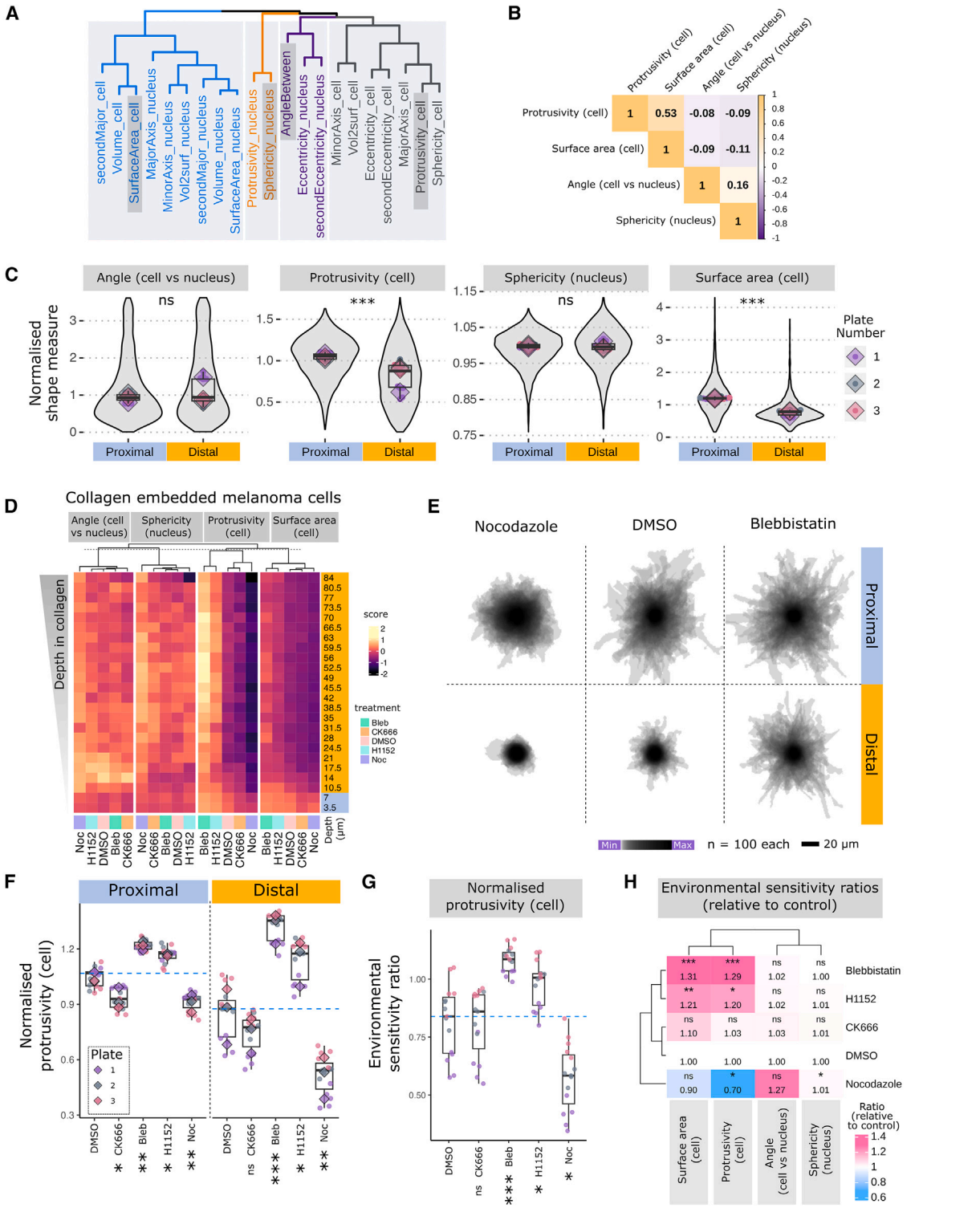

Figure 2. Characteristic shape changes between collagen environments, and interactions between non-muscle myosin II, microtubules, and the collagen environment

Shape changes in WM266-4 cells in collagen hydrogels are shown. Data from De Vries et al.[38]

(A) Hierarchical clustering of shape features based on correlations between features. Selected features are highlighted (dark gray). See Tables S1 and S2 for feature names and descriptions.

(B) Correlation matrix of four selected shape features.

(legend continued on next page)

a protrusivity metric (Figures 1E, 1F, and S1). Increases in the protrusivity metric correlated with direct counts of the number of cell protrusions (Figures S1E and S1F), and linear models predicting protrusivity from the number of protrusions gave an R^2 of ~0.448. Combining protrusion number with cell-surface area (which is sensitive to protrusion length) and orbit (distance between cell and nucleus centers) gave an improved R^2 of ~0.595. Thus, our protrusivity metric is a single measure that captures information about the number of protrusions, cell-surface area, and relative positions of the cell and nucleus.

To visualize the relation of morphology and distance from the rigid coverslip, we generated heatmaps of shape measurements at different depths in collagen on plastic (Figure 1G). We noted changes in protrusivity and other measures depending on whether the base of the nucleus was less than 7 μm (proximal) or greater than 7 μm (distal) from the coverslip, and we categorized each cell as proximal or distal based on this criterion (Figures 1G–1J). This cutoff is consistent with previous studies showing that cells grown on soft layers can undergo shape changes at between 3 and 10 μm distance from an underlying rigid coverslip or surface (depending on substrate and cell line).[44,46,51–53]

Human melanoma cells adopt different shapes in distinct microenvironments

To understand how cells respond to changes in the geometric and physical properties of the environment, we first studied unperturbed proximal and distal cells from our De Vries et al. dataset.[38] A number of our morphology measures were correlated, so we used hierarchical clustering based on correlations between features to generate a reduced set for analysis. Clustering identified four groups of shape features (Figure 2A), and the representative features chosen were "cell surface area," "angle between cell and nucleus," "cell protrusivity," and "nucleus sphericity." The highest absolute correlation between these features was ~0.53 (Figure 2B). Comparison of the morphology of unperturbed proximal and distal cells within the same wells revealed stereotypic differences. Distal cells were typically less protrusive (Figure 2C) and had a smaller surface area (Figure 2C) compared with proximal cells. In contrast to cell-shape features, the nuclear sphericity and angle between the cell and the nucleus were not significantly different between proximal and distal cells. These data reveal that WM266-4 cells make specific and characteristic morphological changes in response to the geometric and physical properties of the microenvironment.

Biology of protrusivity in 3D collagen

To understand how molecular control of protrusions changes between different environments, we used a subset of conditions from De Vries et al.[38] to visualize and test how cell protrusivity is affected by treatment with small-molecule inhibitors of the cytoskeleton (Figures 2D–2H). Treatments included CK666 (Arp2/3 inhibitor), which reduces branched actin polymerization[54,55]; blebbistatin (NMII inhibitor)[56] and H1152 (ROCK inhibitor), which reduce cell contractility[57–59]; and nocodazole (tubulin binding), which disrupts MT assembly dynamics.[60,61]

Each drug had a consistent effect on protrusivity in both proximal and distal contexts. Arp2/3 inhibition (CK666) and MT inhibition (nocodazole) tended to reduce cell protrusivity in both distal and proximal environments. In contrast, impairing NMII-driven contractility (with blebbistatin) increased cell protrusivity (Figures 2D–2F), visually (Figures 2D and 2E) and by tests of well medians (Figure 2F). We calculated an environmental sensitivity ratio (distal/proximal) of protrusivity for each treatment and found striking interactions between the inhibitors of the cytoskeleton and distinct microenvironments. For control (DMSO)-treated cells, this ratio is ~0.84, indicating an ~16% reduction in protrusivity due to changes in microenvironment (Figure 2G). For CK666 treatment, the environmental sensitivity ratio was similar to control at ~0.86. This contrasts with nocodazole, which reduces protrusivity, but with effects that are strongly amplified in the distal environment (ratio of ~0.58). Finally, we found that NMII/ROCK inhibitors increased protrusivity and that their effect was potentiated by the environment (blebbistatin ratio ~1.08 and H1152 ratio ~1.01) (Figure 2G). We extended this test across each shape feature and found corresponding effects of NMII contractility inhibition on surface area (Figure 2H) and small but persistent effects of nocodazole on nucleus sphericity. Notably, untreated WM266-4 melanoma cells reduce protrusivity between proximal and distal environments (Figures 1G and 2C), and inhibiting NMII-based contractility reversed the relationship between microenvironment and protrusivity. NMII-inhibited distal cells were more protrusive than their proximal counterparts. Together these results highlight that protrusivity in 3D-collagen-embedded cells is especially dependent on MTs and especially inhibited by myosin (NMII). The different effects of each inhibitor underscored that WM266-4 cells actively sense and adapt to their environment, with specific dependence on subsets of the cytoskeletal signaling machinery.

(C) Normalized shape features in untreated cells (no treatment) compared between proximal (blue) and distal (orange) cells. Violin plots (gray) are single-cell data. Points and rhomboids are well and plate medians, respectively. Boxplots are from well-level data. Tests are paired Wilcoxon tests, with Benjamini-Hochberg (BH) adjustment at well level. n = 15 pairs per feature.

(D) Heatmaps of shape feature *Z* scores for indicated depths and treatments. Data represent >28,000 cells from three experiments.

(E) Stacked maximum-intensity projections of cell segmentation masks (from a single experimental repeat) that are closest to the median normalized protrusivity for the indicated conditions. Images are log transformed to visualize the range of values. Scale bar: 20 μm.

(F) Normalized cell protrusivity in control and inhibitor treatments. Points and boxplots are well-level data, values are group medians. Rhomboids are from plate medians.

(G) Ratio of distal/proximal protrusivity of each well for the data from (F). Treatments are indicated. Boxplots and points are from well-level data. For (D), (F), and (G), abbreviated treatments are Blebbistatin (Bleb) and Nocodazole (Noc).

(H) Heatmap of environmental sensitivity ratios (distal/proximal) from normalized shape features, with heatmap values and color scale relative to the control (DMSO). Significant differences in environmental sensitivity ratios are indicated. For (C), (F), and (G), point and rhomboid colors indicate plate (experimental repeat). For (F), (G), and (H), tests are Kruskal-Wallis followed by Dunn's *post hoc* compared with control (DMSO), with BH adjustment. n = 15 wells per treatment. Significance levels: ns (no asterisk) $p > 0.05$; *$p < 0.05$; ** $p < 0.01$; ***$p < 0.001$.

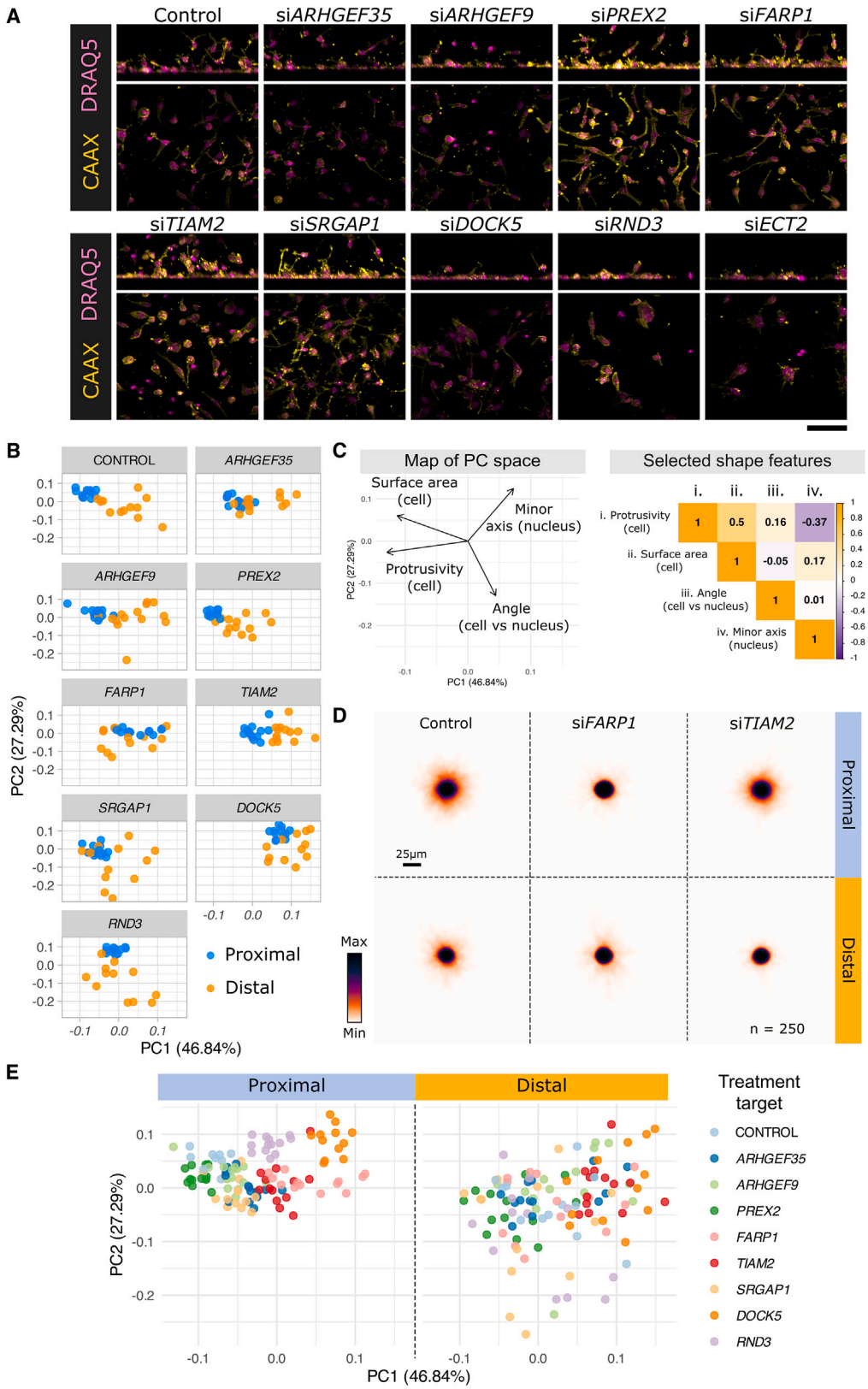

(legend on next page)

RhoGEF/GAP/GTPases contribute to cell morphogenesis in environmentally independent and dependent ways

Our data indicated that cells in fully collagen-embedded (distal) microenvironments reduce their protrusivity, and this effect is modulated in opposing ways by contractility and MT polymerization. To extend this understanding of molecular control of protrusivity, we analyzed RhoGEF, RhoGAP, Rho GTPase, and Rho-GTPase-related genes (RhoGEF/GAP/GTPases) and used genetics to determine whether they control shape differences between microenvironments.

We selected genes for study based on data from our previous quantitative morphological screens depleting the majority of human RhoGEFs and RhoGAPs, and a range of associated genes, on top of collagen matrices or plastic (Figure S2).[62,63] Notably, our measures for already known melanoma shape regulators were consistent with previous screens in derivatives of the A375 cell line.[8,28] In particular, *ARHGAP22* and *DOCK10* depletion increased elongation of cells cultured on top of 3D collagen, whereas *DOCK3* depletion increased cell roundness (Figure S2). We selected the following nine genes for further characterization: *ARHGEF35*, *ARHGEF9*, *PREX2*, *FARP1*, *TIAM2*, *SRGAP1*, *DOCK5*, *RND3*, and *ECT2*.

We depleted these nine RhoGEF/GAP/GTPases (Figure S3) and imaged them in collagen hydrogels on glass via ssOPM (Figure 3A). *ECT2* siRNA functioned as a positive control for transfection efficiency,[64,65] as *ECT2*-depleted cells frequently display a visible multinucleate phenotype due to failed cytokinesis.[66] Penetrance of more than 80% (Figures S3A–S3C) indicated high rates of functional depletion. RT-qPCR for eight of nine of our genes showed on average ~92.9% reduction in transcript with a standard deviation of ~5.8 (Figure S3D). Taken together these data indicate potent target depletion throughout our experiments.

We measured cell morphology and performed dimensionality reduction, which isolated similar representative features (as from the dataset in Figure 2A) except that "nucleus sphericity" clustered differently and was substituted with "nucleus minor axis" (Figures 3C and S4). The general stability of our feature reduction suggested we were tracking *bona fide* structures in the cell geometry feature space. The difference in nuclear feature clustering may relate to differences in nucleus signal and segmentation between DRAQ5 (collagen hydrogel on glass) and Histone-iRFP670 (collagen hydrogel on plastic). Consistent with our results for collagen hydrogels on plastic (Figure 2), control-treated cells had reduced protrusivity and cell-surface area in distal versus proximal environments (Figure S4).

To quantify how RhoGEF/GAP/GTPases affect cell shape in proximal versus distal cells, we projected feature measures (Figure 3B) in principal-component (PC) space (Figure 3C). Protrusivity made a large contribution to PC1, while nucleus minor axis and the angle between the cell and the nucleus made large contributions to PC2. Interestingly, depletion of some RhoGEF/GAP/GTPase genes (for example, *FARP1*) generated overlap between proximal and distal cells in PC space (Figure 3B). We visualized this shape convergence between proximal and distal cells by generating stacked maximum-intensity projections (MIPs) of cell masks (Figure 3D). These data indicated that depletion of *FARP1* uncouples environmental changes from shape control (Figures 3B–3D). In contrast, *TIAM2*-depleted cells appeared increased in PC1 (reduced protrusivity), irrespective of proximal or distal context. This suggests that *TIAM2* regulates shape in environmentally independent ways.

To determine whether the effects of gene depletion on morphology were more potent in proximal or distal environments, we compared the distributions of treatments in PC space for different environments (Figure 3E). RhoGEF/GAP/GTPase-depleted cells in proximal environments were visually separated from control-treated cells (Figure 3E), but in the distal context they were more widely distributed in PC space and overlapped with control (Figure 3E). This indicated that the depletion of RhoGEF/GAP/GTPases has more stereotyped effects on cell shape in proximal (flat) compared with distal (embedded) environments. To understand the source of increased variation in the distal context, we inspected the coefficient of variation (CV) for the control treatment shape features. We noted increased variation in protrusivity for distal cells (Figure S3E), and Fligner tests for homogeneity of variance found that this difference was significant in two of our three replicates (Figure S3F). Fisher's test for combining p values supported the overall significance of the results that the variance in protrusivity increases in distal environments.

Labeling data points by experimental repeats in PC space revealed that a further component of variation (PC1) was batch related (Figure S3G). Interestingly, this batch variation appeared greater in distal cells. One likely source of this variation is differences in the physicochemical properties of collagen between experiments. These data on variability also suggest that the statistical power to differentiate cell phenotypes following gene depletion is greater when cells are proximal versus distal to the coverslip surfaces. Together, these data indicate that greater variability in morphology in distal environments is driven by increased variation in protrusivity and increased sensitivity to the varying properties of the collagen microenvironment.

Figure 3. RhoGEF/GAP/GTPase-related gene depletion disrupts cell shape differences between collagen environments

Treatments are control (CONTROL/Control) or siRNA treatment targeting the indicated gene.

(A) Cropped xy/xz MIPs for nine Rho-regulator siRNA treatments. Cells are marked by CAAX-GFP (yellow) and nuclei by DRAQ5 (magenta). CONTROL example is from the same volume as Figure 1C. Scale bar: 100 μm.

(B) Principal-component analysis (PCA) plots of well medians, based on normalized measures. Proximal (blue) and distal (orange) conditions are indicated. Wells per condition: CONTROL, 12; *ARHGEF35*, 14; *ARHGEF9*, 14; *PREX2*, 13; *FARP1*, 13; *TIAM2*, 13; *SRGAP1*, 13; *DOCK5*, 12; *RND3*, 13.

(C) Biplot of shape features in PC space (left) and feature correlation matrix (right).

(D) Stacked MIPs of segmentation masks of proximal or distal cells for treatment targeting the indicated gene. n = 250 each. Scale bar: 25μm.

(E) PCA of data from (B), highlighting the effects of distal or proximal collagen environments.

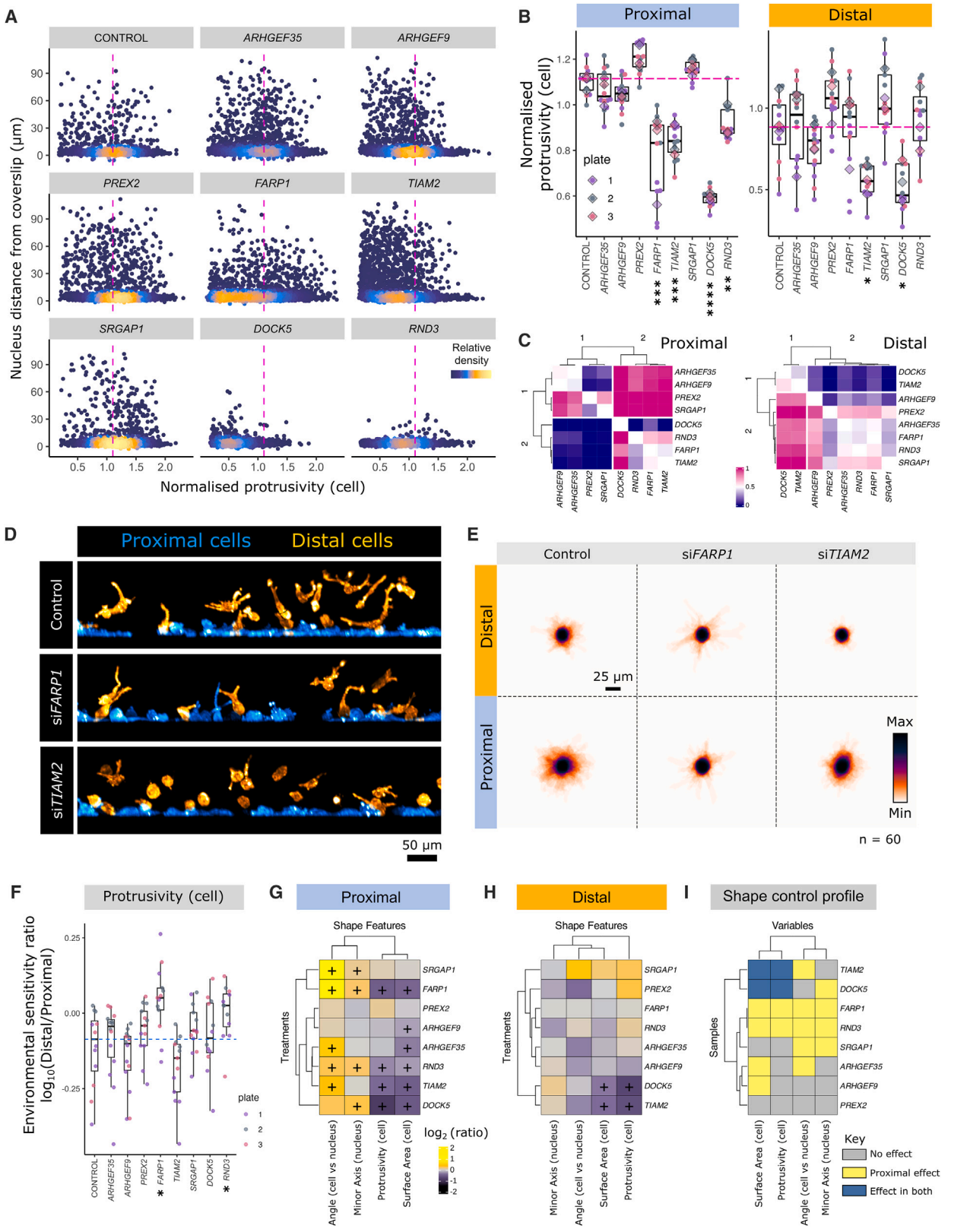

(legend on next page)

The effect of RhoGTPase regulators on cell shape is environmentally constrained

PC analysis and visualization had indicated that some RhoGEF/GAP/GTPases disrupt environmentally dependent morphological changes. Next, we specifically tested their effect on shape features, with a focus on cell protrusivity. We visualized single-cell protrusivity (Figure 4A) and compared the protrusivity of control and RhoGEF/GAP/GTPase-depleted WM266-4 melanoma cells separately for proximal and distal cells (Figures 4B and 4C). In proximal cells, depletion of *FARP1*, *TIAM2*, *DOCK5*, and *RND3* each decreased protrusivity (Figure 4B). In the distal context, only cells depleted for *TIAM2* and *DOCK5* had reduced protrusivity (Figure 4B). We also leveraged the large number of siRNA treatments to look at effects on protrusivity without reference to a control treatment (Figure 4C). We used a W statistic for common language effect size analysis of siRNA treatments on protrusivity and found the same set of genes and patterns of environmental dependence (Figure 4C). Previous screens in melanoma have focused on ameboid (round) to mesenchymal (elongated) shape transitions,[8,28] and we found that gene depletions reducing protrusivity tended to increase sphericity (3D roundness) (Figure S5). We plotted elongation (termed "cell secondEccentricity"), protrusivity, and sphericity (roundness) on ternary plots (Figures S5C–S5E), which highlighted that the round versus elongated dichotomy may not capture differences in cytoskeletal signaling between cells that are elongated and smooth versus elongated and protrusive (Figure S5). These data indicate that depletion of some RhoGEFs (such as *TIAM2* and *DOCK5*) reduces protrusivity in environmentally independent ways. In contrast, depletion of others (such as *FARP1* or *RND3*) does so only in proximal (stiff and flat 3D) environments.

RND3 and *DOCK5* depletion appeared to be associated with a reduction in cell number, suggesting that decreased viability may explain the quantitative decrease in protrusivity (Figure 4A). We therefore focused our analysis on *FARP1* and *TIAM2* and also checked for an influence of apoptotic pathways on shape by measuring cleaved caspase-3 levels in cells depleted for *FARP1* or *TIAM2* (Figure S6). A majority of cells (~96%) had low levels of cleaved caspase-3 (Figures S6A and S6B). For a minority of cells with high cleaved caspase-3, there was no effect on roundness for *FARP1* depletion and some increase in roundness (a 2D surrogate measure for protrusivity) for *TIAM2* depletion ($p < 0.05$). Together these results suggest that in a majority of cells *FARP1* and *TIAM2* control shape independent of changes in cleaved caspase-3.

We visualized protrusivity in *FARP1*-depleted and *TIAM2*-depleted cells (Figures 4D and 4E), and this corroborated that *FARP1*-depleted cells are less protrusive in proximal environments but similar to controls in the distal context. In contrast, *TIAM2*-depleted cells were round in both environmental contexts (Figures 4D and 4E). This was reflected in the environmental sensitivity ratio for protrusivity, which showed significant change for *FARP1* but not *TIAM2* (Figure 4F). Taken together, these results indicate that control of protrusivity by *FARP1* depends on the physical properties of the 3D microenvironment.

Finally, we analyzed median values for all features and compared between proximal and distal environments following the depletion of eight RhoGEF/GAP/GTPases, which highlighted *DOCK5* and *TIAM2* as controlling shape features in both proximal and distal contexts (Figures 4G–4I). In contrast, *FARP1*, *SRGAP1*, *ARHGEF35*, and *RND3* affected multiple shape features, but only in the proximal context (Figures 4G–4I).

Scale of regulation of protrusivity and influence of collagen stiffness

Next, we examined the relationship between depth in collagen versus protrusivity and the range over which *FARP1* and *TIAM2* control protrusivity. We binned cells into 3.5 μm intervals and plotted the mean cell protrusivity for up to ~21 μm from the coverslip (Figure 5A). Compared with control, *FARP1* and *TIAM2* were each required for cell protrusivity in cells with nuclei positioned up to 7 μm from the glass coverslip, but for distances beyond this, only *TIAM2* is required for protrusivity (Figures 5A and 5B). We visualized protrusions at a range of distances from the coverslip in cells depleted for *FARP1* or *TIAM2* (Figures 5C and 5D) and noted that *FARP1*-depleted cells appeared to form hyper-elongated protrusions beginning at ~8–11 μm. *FARP1*-depleted cells also appeared equally as or

Figure 4. Effects of RhoGEF/GAP/GTPase-related gene depletion on protrusivity in different collagen contexts

Treatments are control (CONTROL/Control) or siRNA treatment targeting the indicated gene.

(A) Normalized protrusivity versus nucleus distance from coverslip in single cells for the indicated treatments. Heatmap depicts density. Lines indicate median of control.

(B) Normalized protrusivity for proximal and distal cells under siRNA targeting the indicated genes. Well (points) and plate (rhomboids) medians are indicated. Boxplots are based on well-level data.

(C) Clustering siRNA treatments by common language effect size on protrusivity (based on Wilcoxon rank-sum test between protrusivity) in proximal (left) and distal (right) contexts (STAR Methods).

(D) xz MIPs for the indicated treatments. Pseudocolor indicates proximal (blue hues) and distal (orange hues) cells. Example images are cropped from different regions of the same ssOPM volumes for the corresponding treatments shown in Figure 3A. Scale bar: 50 μm.

(E) Stacked projections of segmentation masks for proximal or distal cells within ±0.5 median absolute deviation (MAD) of median protrusivity for the indicated treatments. n = 60 each. Scale bar: 25 μm.

(F) Log transformed environmental sensitivity ratios (distal/proximal) for the indicated treatments, based on data in (B). Boxplots and points are from well-level data.

(G and H) Heatmaps display ratio ($\log_2$) of shape measures for indicated treatment versus control in proximal (G) or distal (H) contexts. Significance is denoted as "+" where $p < 0.05$ compared with control.

(I) Logical combination of significant changes from (A) and (B). For (B), (F), (G), and (H), tests are Kruskal-Wallis with Dunn's *post hoc* compared with CONTROL, with BH adjustment. Samples are wells, and n are as follows: CONTROL, 12; *ARHGEF35*, 14; *ARHGEF9*, 14; *PREX2*, 13; *FARP1*, 13; *TIAM2*, 13; *SRGAP1*, 13; *DOCK5*, 12; *RND3*, 13. Significance in (B) and (F): ns (no asterisk) $p > 0.05$; *$p < 0.05$; **$p < 0.01$; ***$p < 0.001$; ****$p < 0.0001$. Plots and tests use normalized shape measures.

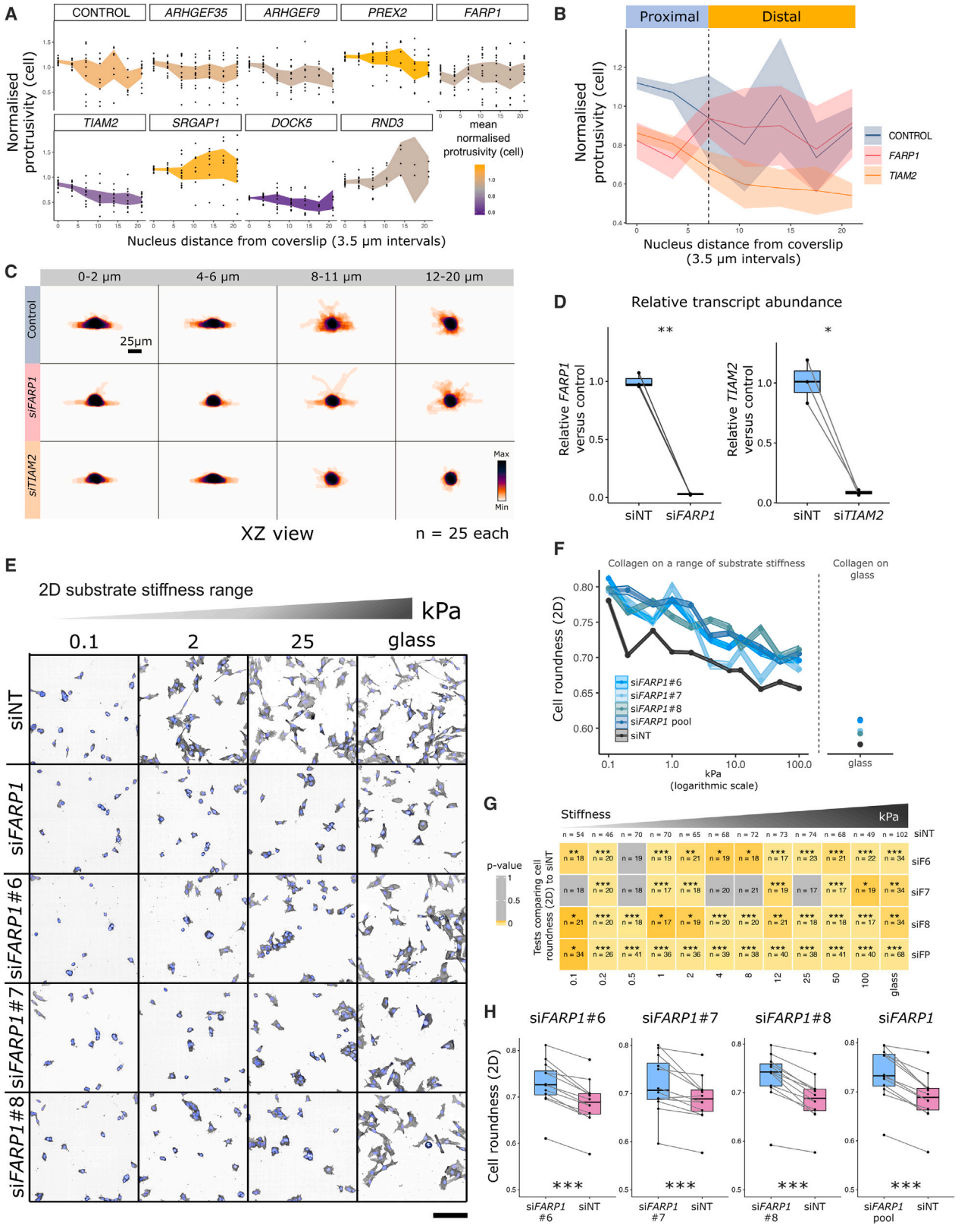

(legend on next page)

more protrusive than control cells at distances beyond 12 μm from the coverslip (Figure 5C). The elongated phenotype suggested that *FARP1* may ordinarily contribute to contractility and rounding in 3D and/or soft (distal) environments. In contrast, *TIAM2* is required for protrusions in both flat/rigid and collagen-embedded/soft environments.

The effect of *FARP1* depletion changed between environments (Figures 4B and 4C), so we tested whether *FARP1* responds to changes in geometry (flat versus fully 3D) and/or stiffness. We examined *FARP1*-depleted cells cultured on 2D collagen-coated substrates across a range of stiffnesses (approximately 0.1–100 kPa) and also collagen-coated glass (Figures 5E–5H). We used pooled siRNAs and three separate siRNAs targeting *FARP1*. In this 2D setting, we measured cell roundness as a surrogate for protrusivity (STAR Methods) (Figures 2A and S4A). Consistent with 3D proximal cells (Figures 5A–5C), *FARP1* depletion on 2D collagen increased cell roundness. We did not find a clear modulating effect of stiffness in *FARP1*-depleted cells (Figure 5F), suggesting that the phenotype of *FARP1* depletion incorporates some response to geometry (2D versus 3D).

We also tested the function of *FARP1* and *TIAM2* in the A375 melanoma cells (Figure S6). Consistent with our results in WM266-4 melanoma, both depletions increased roundness and the related width-to-length ratio (W/L) on 2D surfaces. Notably, the increased W/L ratio between siNT and si*FARP* treatments was amplified by coating tissue-culture plastic with a thin layer of collagen (5–10 $\mu g/cm^2$) (Figure S6H).

Interaction of *FARP1* and *TIAM2* with cell contractility signaling

Depletion of *TIAM2* or *FARP1* in proximal cells, and *TIAM2* in distal cells, leads to reduced protrusivity and increased rounding (Figures 4B and 4D), which is characteristic of ameboid cells. Ameboid migration is largely driven by the formation of blebs, whereby the cell membrane separates from the actin cortex to form a hydrostatic bubble. Blebbing is driven by RHOA-ROCK-NMII-based contractility.[67] To determine whether rounding in *TIAM2*-depleted and *FARP1*-depleted cells was due to NMII upregulation, we assayed blebs in control-, si*FARP1*-, and si*TIAM2*-treated cells (Figures 6A and 6C). We examined raw (non-downsampled) ssOPM images and calculated the proportion of cells with blebs by blinded scoring. At baseline, ~2.3% of control cells were blebbing, whereas *TIAM2* depletion increased the frequency of blebbing (~5.5%) (Figures 6A and 6C). *FARP1*-depleted cells did not have increased blebbing. This suggests that *TIAM2* depletion, but not *FARP1* depletion, leads to round cells because of an upregulation of NMII-dependent contractility and/or suppression of protrusions.

Because a subpopulation of *FARP1*-depleted cells showed elongated protrusions in the distal context (Figure 5C), we scored the presence of highly elongated cells with rear polarized nuclei. These were ~10% in *FARP1*-depleted cells and ~1% or less in control and si*TIAM2*-treated cells (Figure 6B). This suggested that *FARP1* regulates protrusion and contractility independent of NMII and in a non-redundant fashion to *TIAM2*.

To investigate the hypothesis that depletion of *TIAM2*, but not *FARP1*, upregulates NMII contractility, we plated siNT-, si*FARP1*-, and si*TIAM2*-treated WM266-4 in 2D on collagen-coated plastic and treated with control (DMSO) or NMII inhibitor (25μM blebbistatin) (Figures 6D and 6E). Consistent with reduced protrusivity in 3D proximal cells, *FARP1*-depleted, and *TIAM2*-depleted cells increased roundness compared with siNT controls (Figure 6D). In both cases, blebbistatin treatment reduced the extent of roundness (Figure 6D) and the W/L ratio (Figure 6E). *TIAM2*-depleted cells had the strongest response to blebbistatin and the greatest decrease in rounding (Figure 6D). Visually, blebbistatin-treated siNT cells had elongated protrusions, whereas blebbistatin-treated *TIAM2*-depleted cells resembled the controls (Figures 6F and 6G). These data are consistent with a model where *TIAM2* depletion leads to increased levels of RHOA and NMII activation, such that NMII inhibition by blebbistatin treatment can rescue the si*TIAM2* rounded phenotype.

Environmental interaction of *TIAM2* expression with cell shape

To understand the role of *TIAM2* and *FARP1* in cell morphogenesis we expressed mCitrine-YFP (YFP)-tagged versions of these proteins in 2D tissue culture and measured the effect of transgene expression on cell "shape parameter" on different

Figure 5. Length scale for environmental effect on protrusivity, and influence of stiffness on shape

Genetic treatments are control (CONTROL or siNT) or siRNA treatment targeting the indicated gene.

(A) Normalized protrusivity versus nucleus distance from coverslip for each treatment. Points are well medians. Ribbon extent indicates 90% confidence interval, and color indicates mean. Observation number at each interval is indicated by number of points.

(B) Overlay of indicated treatments from Figure 1A. Lines indicate means of well medians, and ribbon extent indicates 90% confidence interval.

(C) Stacked xz MIPs of segmentation masks at indicated distances from coverslip for cells within ±1 median absolute deviation (MAD) of median protrusivity. Scale bar: 25 μm.

(D) RT-qPCR measures for indicated treatments. Boxplots and paired points are shown. Tests are paired t tests, n = 3 pairs each. n is the mean of replicates from different cDNA concentrations, following a single knockdown and RNA extraction.

(E) Confocal images of WM266-4 cells on varied stiffnesses (indicated as kPa or glass) of 2D collagen surfaces with specified treatments. Actin, inverted gray scale; DNA, blue. Scale bar: 100 μm.

(F and G) Plotting and tests of difference in cell roundness from the same experiment as in (E). For cell numbers see STAR Methods. (F) Semi-log plot (left facet) of cell roundness versus stiffness (kPa, in log-10 scale). Points are mean cell roundness, connected by lines. Ribbon widths indicate standard error of the mean (±SEM). The x-axis scale is discontinuous for the last stiffness condition (collagen-coated glass). (G) Tests of roundness differences (from data in F) versus control at the indicated stiffnesses. Kruskal-Wallis tests followed by Dunn tests with BH adjustment were conducted at the field-of-view (FOV) level from one experiment, and n values represent FOVs. *FARP1* depletion is indicated as pooled (siFP) or deconvoluted siRNA ("siF" followed by an ID number).

(H) Comparison of mean roundness for stiffness-matched pairs for each treatment versus the same siNT control. Point values are mean roundness for the indicated condition, and boxplots are based on these. Tests are Wilcoxon tests on paired samples, with BH adjustment. Sample numbers are n = 12 pairs. Significances in (D), (G), and (H): ns (no asterisk) $p > 0.05$; *$p < 0.05$; **$p < 0.01$; ***$p < 0.001$.

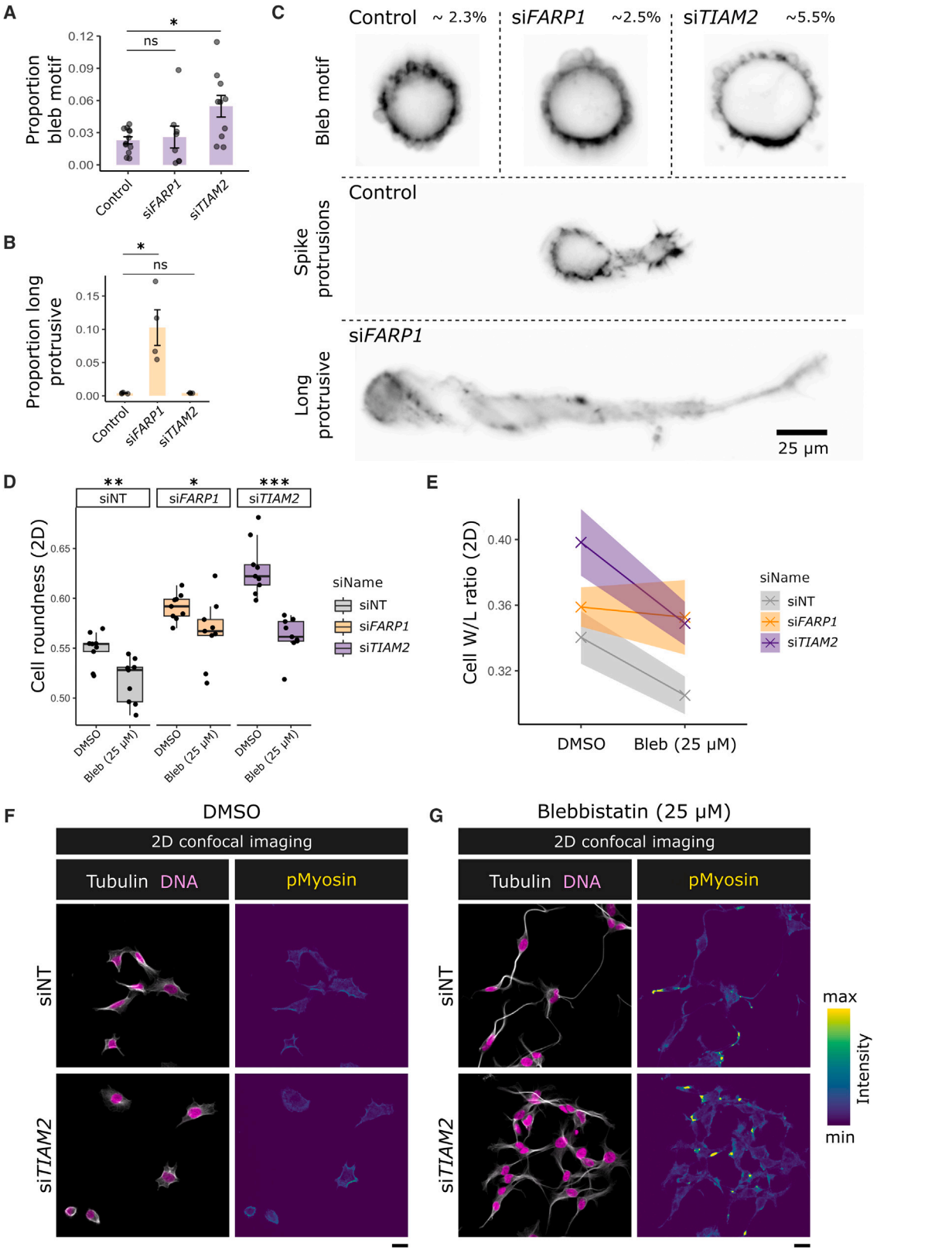

(legend on next page)

substrates (Figures 7A–7D). Shape parameter is a commonly used metric with a lower limit defined by circular shapes and increases with higher surface-to-area ratio (Figure 7B).[68–70] We used a *Z* score fluorescence intensity threshold to define transgene-expressing cells (labeled as "on") and compared their shape parameter with non-expressing counterparts in the same well (labeled as "off") (Figure 7C) (STAR Methods). We also compared the effects on both tissue-culture plastic ("tc" in Figure 7D) and collagen-coated plates ("Col1" in Figure 7D). These experiments were in two biological repeats comparing a combined total of >400,000 expressing and non-expressing cells (see STAR Methods).

Expression of a GFP control, or YFP-FARP1, had either minimal or no detectable effects on cell shape parameter (Figure 7C). However, YFP-TIAM2 (mouse sequence) expression had some notable effects. First, YFP-TIAM2-expressing cells had reduced shape parameter (Figure 7C). Second, the effect of YFP-TIAM2 was context dependent and stronger on collagen versus plastic substrates (Figure 7D). Third, we saw a specific perinuclear localization of YFP-TIAM2 (Figures 7A, 7E, and 7F) in line with the localization reported by others with independent *TIAM2* transgenes.[71] We scored the phenotype of all YFP-TIAM2-expressing cells (n = 62) for predominance of filaments (~56%), ruffles (~32%), or blebs (~11%) (Figure 7F). We noted higher proportions of blebs and ruffles compared with a survey of GFP-expressing cells (n = 46), which bore mostly filaments (~91%) and fewer ruffles (~7%) or blebs (~2%). The frequent presence of ruffling in YFP-TIAM2-expressing cells was consistent with Rac1 activation.

A model of environmental shape modulation

Taken together, the results of this study begin to delineate a model of broad-acting and context-specific regulators of 3D cell protrusivity (Figure 7G). Regarding the cytoskeleton, we find environmental potentiation of the roles of NMII activation and MTs versus Arp2/3-dependent branched actin. For RhoGEF/GAP/GTPase proteins we find two RhoGEFs that are examples of broad (*TIAM2*) and context-specific (*FARP1*) regulation of protrusivity (Figure 7G).

DISCUSSION

Cell response to physical properties of the microenvironment

Our 3D ssOPM analysis used cells seeded into collagen hydrogels on top of glass or plastic. We interpret this setup as creating an effective "stiffness gradient," where the elastic properties of the collagen proximal (near) to the glass or plastic are influenced by the rigidity of the underlying substrate, whereas cells distal (far) from this substrate experience the greater elasticity of the collagen. Effective stiffness gradients in hydrogels of uniform physical composition have been studied in the context of soft materials placed on rigid substrates.[46,53] A key finding is that material displacement in soft gels is affected by distance from an underlying rigid material and that this influence decreases rapidly with distance.[52] In line with this, many studies have shown that the spreading behavior of cells increases on stiff versus soft materials and that cells grown on nominally soft gels are influenced by the presence of an underlying rigid substrate.[44,46,51–53,72]

The literature suggests that the mechanical influence of an underlying substrate begins to decay after a few micrometers (smaller than the scale of a cell) but can extend beyond 100 μm (larger than the scale of many cell types). The range of influence depends on the composition of the gel, cell type, and readout of physical sensing. For this study we used rat tail collagen 1[17]; however, collagen hydrogels from different sources vary in physical properties.[18,19] For example, rat tail is considered minimally cross-linked compared with bovine, in practice having shorter fibers and smaller pores than other collagen sources.[19,20]

We tracked multiple cell morphology features and found decreases in protrusivity and cell-surface area when nuclei were about 7 μm from the coverslip, indicating diminished influence of the rigid substrate over this distance. The average nuclear diameter in our 3D glass well dataset was close to 16 μm, meaning that cells respond to changes in the physical environment over scales that are smaller than the dimensions of the nucleus. The nucleus is known to have mechanosensing properties[73,74] and is a major mechanosensing compartment of the cell. It will be interesting to determine whether it is the cell or the nucleus that is sensing and responding to the physical environment at different distances from a rigid substrate.[2,3]

Environmentally dependent control of cell protrusivity by *TIAM2*, *FARP1*, and the cytoskeleton

Rho GTPases are central to cell shape regulation and are modulated by RhoGEFs and RhoGAPs. We hypothesize that identifying RhoGEFs/GAPS that control 3D morphology remains challenging because, compared with the ~20 Rho GTPases, many of the ~145 human RhoGEFs/GAPs may have subtle or context-dependent effects on cell morphology. Focusing on

Figure 6. Effects of *FARP1* and *TIAM2* depletion on morphological motifs, and interaction with contractility signaling

Genetic treatments are control (CONTROL/Control or siNT) or siRNA treatment targeting the indicated gene.

(A and B) Proportion of blebbing (A) and long protrusive cells (B) per treatment. Points are well proportions, and bars are mean ± standard error. Tests are Kruskal-Wallis and *post hoc* Dunn's test with BH adjustment. Sample sizes: (A) CONTROL, 12; *FARP1*, 8; *TIAM2*, 12; (B) CONTROL, 4; *FARP1*, 4; *TIAM2*, 3.

(C) Cropped images of bleb motifs for each treatment (top row). Comparison of control (Control) protrusive versus si*FARP1* long protrusive (bottom two rows). Image intensity is scaled separately for each image. Scale bar: 25 μm.

(D) Points represent wells, and are median cell roundness for the indicated siRNA and blebbistatin (Bleb; 25 μM) treatments. Boxplots are based on well-level data. Tests are Wilcoxon tests, with BH adjustment. Sample numbers: n = 9 wells for each condition.

(E) Width-to-length (W/L) ratio for indicated treatments from the same experiment as in (D). Line is the mean of well means, and ribbon indicates ±standard deviation. Sample numbers: n = 9 wells per condition.

(F and G) Cropped confocal images of WM266-4 melanoma under the indicated treatments from the experiment in (D) and (E). Tubulin, gray; DNA, magenta; and phosphorylated myosin regulatory light chain (pMyosin), viridis palette. Intensity palette applies to (F) and (G). Scale bars: (F and G) 50 μm. For (A), (B), and (D), significance levels are ns $p > 0.05$; *$p < 0.05$; **$p < 0.01$; ***$p < 0.001$.

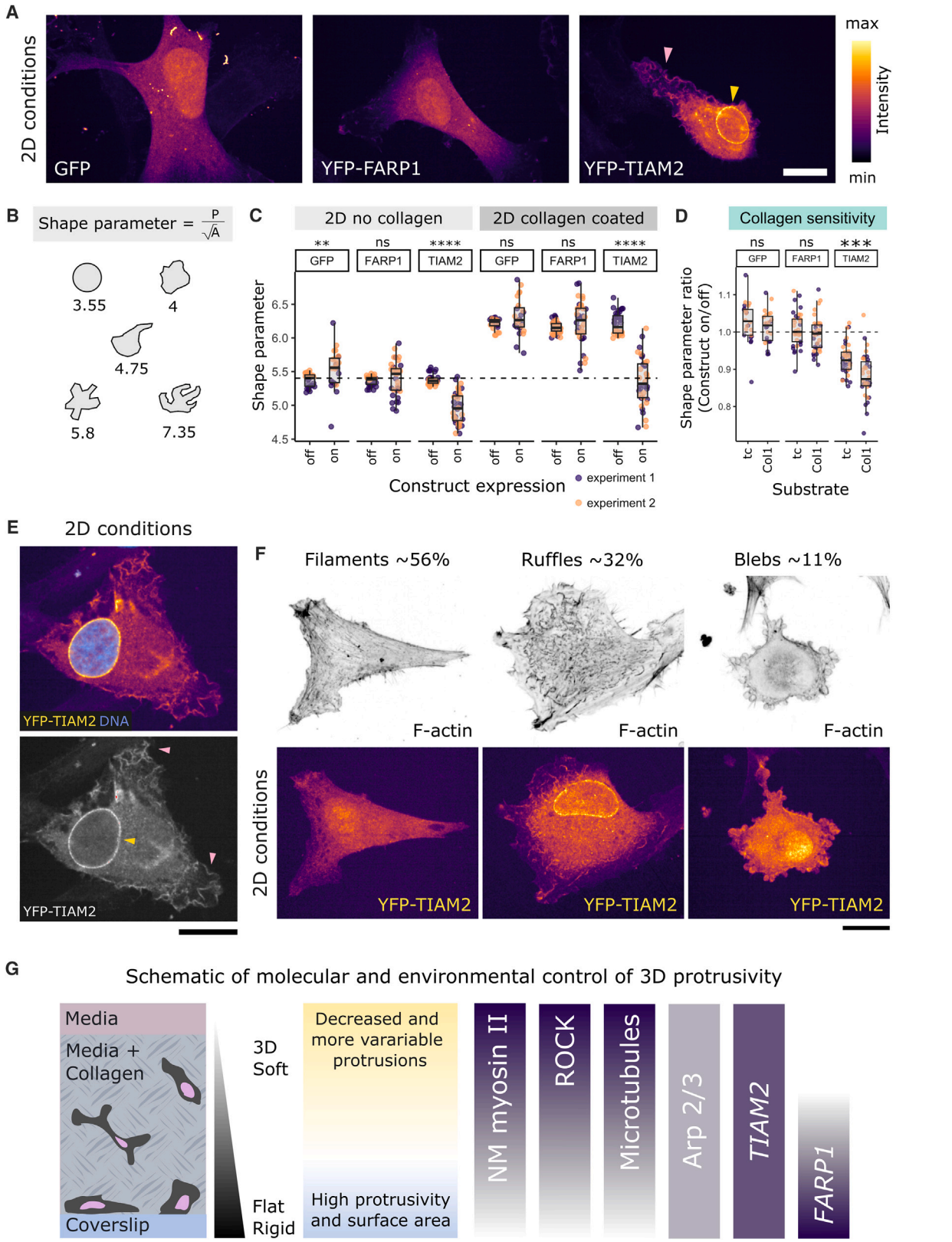

(legend on next page)

protrusivity and depth in collagen, we highlighted *FARP1* as having context-dependent effects versus *TIAM2*.

TIAM2 is a Rac1 GEF,[30,75,76] and the reduced 3D protrusivity following *TIAM2* depletion was similar to the Arp2/3 inhibitor CK666. This is consistent with a model where TIAM2 activates RAC1 to promote Arp2/3-dependent actin protrusions.[77] *TIAM2*-depleted cells also had increased rounding in 2D that depends (at least in part) on NMII and increased 3D blebbing compared with control cells (Figures 6A, 6C, and 6D). These phenotypes are consistent with RHOA activation. There is a known antagonism between RAC1 and RHOA activation[78–81]; thus, a TIAM2-RAC1 axis might deactivate RHOA either directly or indirectly.

TIAM2 overexpression in 2D reduced the shape parameter (Figure 7B) and often appeared associated with membrane ruffling (Figure 7F). *TIAM2* has been shown to activate RAC1; aid in the formation of perinuclear actin caps,[71] actin-rich membrane ruffles,[75] and actin-mediated *trans*-endocytosis[82]; and promote focal adhesion disassembly.[83] We reason that the reduced shape complexity when *TIAM2* is overexpressed could result from RAC1-mediated lamella formation,[84] or focal adhesion disassembly,[83] versus the blebbing and NMII-dependent rounding from *TIAM2* depletion.

FARP1 promotes dendritic growth and arborization,[85–87] synapse morphogenesis,[87] actin-rich tunneling nanotubes,[88] and stabilization of the endothelial barrier.[89] In different cell types FARP1 appears to act upstream of both RAC1[75,87] and CDC42.[88–90] We observed that *FARP1* depletion resulted in context-dependent morphologies and, in particular, microenvironmental geometry (flat versus fully 3D embedded). As with *TIAM2*, depletion of *FARP1* resulted in cell rounding in 2D, but is unlikely to be associated with increased actomyosin contractility, as *FARP1* did not change rates of blebbing. Given that FARP1 is a CDC42 activator, a possible cause of context dependence is that *FARP1*-depleted cells near to the coverslip cannot extend filopodia to make adhesion-dependent protrusions, whereas protrusions distal to the coverslip may be independent of filopodia. Finally, our study revealed potentiating interactions between the 3D microenvironment and ROCK-NMII and between the microenvironment and MTs. This raises the possibility that crosstalk and antagonism between ROCK-NMII and MTs[91,92] have a greater influence on cell contractility and protrusion formation in soft/fully 3D environments versus stiff/flat environments.

Limitations of the study

Our exploration focused on the WM266-4 cell line with some 2D validation in A375 melanoma cells. It will be useful to determine the generality of these findings in other models, such as lung adenocarcinoma and endothelial cells, where *TIAM2* and *FARP1* regulate motility and barrier function.[84,89] Our imaging method revealed regulators of morphology via a static view. However, multiple-time-point live imaging will be required to determine how cytoskeleton inhibition and RhoGEF/GAP/GTPase depletion affect migration between environments and how this correlates with morphology.

STAR★METHODS

Detailed methods are provided in the online version of this paper and include the following:

- KEY RESOURCES TABLE
- RESOURCE AVAILABILITY
  - Lead contact
  - Materials availability
  - Data and code availability
- EXPERIMENTAL MODEL AND STUDY PARTICIPANT DETAILS
- METHOD DETAILS
  - Cell culture
  - Cell preparation for imaging, siRNA and inhibitor treatments
  - Stage-scanning oblique plane microscopy (ssOPM) setup
  - ssOPM image acquisition
  - ssOPM image reslicing and registration
  - ssOPM image segmentation
  - ssOPM image measures
  - Confirmation that shape changes between environments are robust to segmentation method and ssOPM light sheet PSF shape
  - Measuring 3D collagen environment by scattered light intensity
  - ssOPM data processing
  - ssOPM maximum intensity projections for example visualisation

Figure 7. Phenotypes and environmental modulation of *FARP1* and *TIAM2* expression

(A) Cropped images of cells on 2D collagen expressing the indicated transgene-encoded proteins. Perinuclear YFP-TIAM2 (yellow arrowhead) and membrane ruffles (pink arrowhead) are indicated. Scale bar: 20 μm. Inferno color scale is used throughout.

(B) Schematic depicting shape parameter metric.

(C) Points represent shape parameter medians for each well. Gene expression treatments are *GFP* (GFP), *YFP-FARP1* (FARP1), and *YFP-TIAM2* (TIAM2). Transgene expressing (on) and non-expressing (off) conditions, and also collagen conditions are indicated. Boxplots are based on well data.

(D) Points represent wells and are shape parameter ratios between expressing and non-expressing cells for data in (C). Tests compare the ratios for cells on 2D plastic (tc) versus 2D collagen (Col1). Boxplots are based on well data. For (C) and (D), colors (purple and orange) indicate experimental repeats, and statistics are Wilcoxon tests, with BH adjustment. Sample numbers for each condition in (C) and (D) are *GFP* (GFP) treatments, n = 24; *YFP-FARP1* (FARP1), n = 36; *YFP-TIAM2* (TIAM2), n = 36. For (C) and (D), significance levels are ns $p > 0.05$; ** $p < 0.01$; *** $p < 0.001$; **** $p < 0.0001$.

(E) Cropped image of YFP-TIAM2-expressing cell. Top: YFP-TIAM2 (inferno palette) and DNA (blue). Bottom: YFP-TIAM2 (gray). Perinuclear YFP-TIAM2 (yellow arrowhead), membrane ruffling (pink arrowheads), and saturated pixels (red) are indicated. Scale bar: 20 μm.

(F) Cropped images of YFP-TIAM2-expressing cells and proportions of indicated phenotypes (n = 62). F-actin, inverted gray scale, and YFP-TIAM2, inferno palette. Scale bar: 20 μm.

(G) Schematic summarizing molecular and environmental influences on protrusivity. Lower (gray) and higher (purple) influence is indicated. Non-muscle myosin II (NM myosin II).

- Bleb and elongation assay from raw ssOPM data
- ssOPM data visualisations, stacked maximum intensity projections, heatmaps and general plotting
- Plotting of preliminary screens of shape regulation
- 2D imaging, measurements, and assays
- Measurements for 2D substrates at a range of stiffness
- *FARP1* and *TIAM2,* 2D expression assay
- Real time quantitative PCR
- Immunostaining and dye staining
- Statistical methodology
- ssOPM statistical data analysis
- W-statistic for common language effect size analysis of siRNA treatments on protrusivity

- QUANTIFICATION AND STATISTICAL ANALYSIS

SUPPLEMENTAL INFORMATION

Supplemental information can be found online at https://doi.org/10.1016/j.celrep.2024.114016.

ACKNOWLEDGMENTS

This work was funded by a UK Engineering and Physical Sciences Research Council Impact Acceleration grant (EP/K503733/1), a Cancer Research UK Multidisciplinary Project Award (C53737/A24342), a Cancer Research UK funded Accelerator Award (A29368), and The UK Terry Fox Association. C.B. is funded by a Cancer Research UK and Stand Up to Cancer UK Programme Foundation Award (C37275/1A20146). The authors wish to acknowledge the expert help of Martin Kehoe and Simon Johnson in the Optics Workshop of Imperial College Photonics Group who contributed to the design and fabrication of components for the ssOPM, and the Institute of Cancer Research Light Microscopy Facility. We are grateful to Oliver Rocks for providing *FARP1* and *TIAM2* plasmids.

AUTHOR CONTRIBUTIONS

Writing and conceptualization were by L.G.D., N.C., C.D., and C.B., with contributions to editing by F.B., M.A.-G., and H.S. Formal analysis by was L.G.D., N.C., I.J., M.A.-G., C.B., and C.D. Experimental investigation was by L.G.D., V.B., M.A.-G., and F.B. Optimization of siRNA transfections and preparation of cells in collagen for glass well plates for ssOPM imaging were by M.A.-G. ssOPM imaging, segmentation, and measurement were by N.C., H.S., and L.R.-B. Development of the ssOPM system and image processing code was by V.M., S.K., I.M., N.C., H.S., L.R.-B., and C.D.

DECLARATION OF INTERESTS

C.D. has a licensed granted patent on the optical arrangement for oblique plane microscopy (OPM) under patent nos. US 8582203 B2 and EP 2316048 B1.

Received: January 30, 2023
Revised: March 4, 2024
Accepted: March 14, 2024
Published: April 17, 2024

REFERENCES

1. Geiger, B., Spatz, J.P., and Bershadsky, A.D. (2009). Environmental sensing through focal adhesions. Nat. Rev. Mol. Cell Biol. *10*, 21–33. https://doi.org/10.1038/nrm2593.
2. Venturini, V., Pezzano, F., Castro, F.C., Häkkinen, H.-M., Jiménez-Delgado, S., Colomer-Rosell, M., Marro, M., Tolosa-Ramon, Q., Paz-López, S., Valverde, M.A., et al. (2020). The nucleus measures shape changes for cellular proprioception to control dynamic cell behavior. Science *370*. https://doi.org/10.1126/science.aba2644.
3. Lomakin, A.J., Cattin, C.J., Cuvelier, D., Alraies, Z., Molina, M., Nader, G.P.F., Srivastava, N., Sáez, P.J., Garcia-Arcos, J.M., Zhitnyak, I.Y., et al. (2020). The nucleus acts as a ruler tailoring cell responses to spatial constraints. Science *370*, eaba2894. https://doi.org/10.1126/science.aba2894.
4. Martino, F., Perestrelo, A.R., Vinarský, V., Pagliari, S., and Forte, G. (2018). Cellular Mechanotransduction: From Tension to Function. Front. Physiol. *9*, 824. https://doi.org/10.3389/fphys.2018.00824.
5. Kechagia, J.Z., Ivaska, J., and Roca-Cusachs, P. (2019). Integrins as biomechanical sensors of the microenvironment. Nat. Rev. Mol. Cell Biol. *20*, 457–473. https://doi.org/10.1038/s41580-019-0134-2.
6. Spill, F., Reynolds, D.S., Kamm, R.D., and Zaman, M.H. (2016). Impact of the physical microenvironment on tumor progression and metastasis. Curr. Opin. Biotechnol. *40*, 41–48. https://doi.org/10.1016/j.copbio.2016.02.007.
7. Sahai, E., and Marshall, C.J. (2003). Differing modes of tumour cell invasion have distinct requirements for Rho/ROCK signalling and extracellular proteolysis. Nat. Cell Biol. *5*, 711–719. https://doi.org/10.1038/ncb1019.
8. Sanz-Moreno, V., Gadea, G., Ahn, J., Paterson, H., Marra, P., Pinner, S., Sahai, E., and Marshall, C.J. (2008). Rac Activation and Inactivation Control Plasticity of Tumor Cell Movement. Cell *135*, 510–523. https://doi.org/10.1016/j.cell.2008.09.043.
9. Wolf, K., Mazo, I., Leung, H., Engelke, K., von Andrian, U.H., Deryugina, E.I., Strongin, A.Y., Bröcker, E.B., and Friedl, P. (2003). Compensation mechanism in tumor cell migration: mesenchymal-amoeboid transition after blocking of pericellular proteolysis. J. Cell Biol. *160*, 267–277. https://doi.org/10.1083/jcb.200209006.
10. Lämmermann, T., and Sixt, M. (2009). Mechanical modes of 'amoeboid' cell migration. Curr. Opin. Cell Biol. *21*, 636–644. https://doi.org/10.1016/j.ceb.2009.05.003.
11. Petrie, R.J., and Yamada, K.M. (2012). At the leading edge of three-dimensional cell migration. J. Cell Sci. *125*, 5917–5926. https://doi.org/10.1242/jcs.093732.
12. Reversat, A., Gaertner, F., Merrin, J., Stopp, J., Tasciyan, S., Aguilera, J., de Vries, I., Hauschild, R., Hons, M., Piel, M., et al. (2020). Cellular locomotion using environmental topography. Nature *582*, 582–585. https://doi.org/10.1038/s41586-020-2283-z.
13. Wolf, K., Müller, R., Borgmann, S., Bröcker, E.B., and Friedl, P. (2003). Amoeboid shape change and contact guidance: T-lymphocyte crawling through fibrillar collagen is independent of matrix remodeling by MMPs and other proteases. Blood *102*, 3262–3269. https://doi.org/10.1182/blood-2002-12-3791.
14. Yamada, K.M., and Sixt, M. (2019). Mechanisms of 3D cell migration. Nat. Rev. Mol. Cell Biol. *20*, 738–752. https://doi.org/10.1038/s41580-019-0172-9.
15. Liu, Y.-J., Le Berre, M., Lautenschlaeger, F., Maiuri, P., Callan-Jones, A., Heuzé, M., Takaki, T., Voituriez, R., and Piel, M. (2015). Confinement and low adhesion induce fast amoeboid migration of slow mesenchymal cells. Cell *160*, 659–672. https://doi.org/10.1016/j.cell.2015.01.007.
16. Ruprecht, V., Wieser, S., Callan-Jones, A., Smutny, M., Morita, H., Sako, K., Barone, V., Ritsch-Marte, M., Sixt, M., Voituriez, R., and Heisenberg, C.P. (2015). Cortical contractility triggers a stochastic switch to fast amoeboid cell motility. Cell *160*, 673–685. https://doi.org/10.1016/j.cell.2015.01.008.
17. Elsdale, T., and Bard, J. (1972). COLLAGEN SUBSTRATA FOR STUDIES ON CELL BEHAVIOR. J. Cell Biol. *54*, 626–637.
18. Abraham, L.C., Zuena, E., Perez-Ramirez, B., and Kaplan, D.L. (2008). Guide to collagen characterization for biomaterial studies. J. Biomed. Mater. Res. B Appl. Biomater. *87*, 264–285. https://doi.org/10.1002/jbm.b.31078.

19. Antoine, E.E., Vlachos, P.P., and Rylander, M.N. (2014). Review of Collagen I Hydrogels for Bioengineered Tissue Microenvironments: Characterization of Mechanics, Structure, and Transport. Tissue Eng. Part B Rev. *20*, 683–696. https://doi.org/10.1089/ten.teb.2014.0086.

20. Wolf, K., Alexander, S., Schacht, V., Coussens, L.M., von Andrian, U.H., van Rheenen, J., Deryugina, E., and Friedl, P. (2009). Collagen-based cell migration models in vitro and in vivo. Semin. Cell Dev. Biol. *20*, 931–941. https://doi.org/10.1016/j.semcdb.2009.08.005.

21. Brábek, J., Mierke, C.T., Rösel, D., Veselý, P., and Fabry, B. (2010). The role of the tissue microenvironment in the regulation of cancer cell motility and invasion. Cell Commun. Signal. *8*, 22. https://doi.org/10.1186/1478-811X-8-22.

22. Yin, Z., Sadok, A., Sailem, H., McCarthy, A., Xia, X., Li, F., Garcia, M.A., Evans, L., Barr, A.R., Perrimon, N., et al. (2013). A Screen for Morphological Complexity Identifies Regulators of Switch-like Transitions between Discrete Cell Shapes. Nat. Cell Biol. *15*, 860–871. https://doi.org/10.1038/ncb2764.

23. Lawson, C.D., and Ridley, A.J. (2018). Rho GTPase signaling complexes in cell migration and invasion. J. Cell Biol. *217*, 447–457. https://doi.org/10.1083/jcb.201612069.

24. Ridley, A.J. (2015). Rho GTPase signalling in cell migration. Curr. Opin. Cell Biol. *36*, 103–112. https://doi.org/10.1016/j.ceb.2015.08.005.

25. Amano, M., Nakayama, M., and Kaibuchi, K. (2010). Rho-Kinase/ROCK: A Key Regulator of the Cytoskeleton and Cell Polarity. Cytoskeleton (Hoboken). *67*, 545–554. https://doi.org/10.1002/cm.20472.

26. Amano, M., Ito, M., Kimura, K., Fukata, Y., Chihara, K., Nakano, T., Matsuura, Y., and Kaibuchi, K. (1996). Phosphorylation and Activation of Myosin by Rho-associated Kinase (Rho-kinase). J. Biol. Chem. *271*, 20246–20249. https://doi.org/10.1074/jbc.271.34.20246.

27. Bisi, S., Disanza, A., Malinverno, C., Frittoli, E., Palamidessi, A., and Scita, G. (2013). Membrane and actin dynamics interplay at lamellipodia leading edge. Curr. Opin. Cell Biol. *25*, 565–573. https://doi.org/10.1016/j.ceb.2013.04.001.

28. Gadea, G., Sanz-Moreno, V., Self, A., Godi, A., and Marshall, C.J. (2008). DOCK10-Mediated Cdc42 Activation Is Necessary for Amoeboid Invasion of Melanoma Cells. Curr. Biol. *18*, 1456–1465. https://doi.org/10.1016/j.cub.2008.08.053.

29. Woodham, E.F., Paul, N.R., Tyrrell, B., Spence, H.J., Swaminathan, K., Scribner, M.R., Giampazolias, E., Hedley, A., Clark, W., Kage, F., et al. (2017). Coordination by Cdc42 of Actin, Contractility, and Adhesion for Melanoblast Movement in Mouse Skin. Curr. Biol. *27*, 624–637. https://doi.org/10.1016/j.cub.2017.01.033.

30. Müller, P.M., Rademacher, J., Bagshaw, R.D., Wortmann, C., Barth, C., van Unen, J., Alp, K.M., Giudice, G., Eccles, R.L., Heinrich, L.E., et al. (2020). Systems analysis of RhoGEF and RhoGAP regulatory proteins reveals spatially organized RAC1 signalling from integrin adhesions. Nat. Cell Biol. *22*, 498–511. https://doi.org/10.1038/s41556-020-0488-x.

31. Nakamura, M., Verboon, J.M., and Parkhurst, S.M. (2017). Prepatterning by RhoGEFs governs Rho GTPase spatiotemporal dynamics during wound repair. J. Cell Biol. *216*, 3959–3969. https://doi.org/10.1083/jcb.201704145.

32. Rossman, K.L., Der, C.J., and Sondek, J. (2005). GEF means go: turning on RHO GTPases with guanine nucleotide-exchange factors. Nat. Rev. Mol. Cell Biol. *6*, 167–180. https://doi.org/10.1038/nrm1587.

33. Tcherkezian, J., and Lamarche-Vane, N. (2007). Current knowledge of the large RhoGAP family of proteins. Biol. Cell *99*, 67–86. https://doi.org/10.1042/BC20060086.

34. Kutys, M.L., and Yamada, K.M. (2014). An extracellular matrix-specific GEF-GAP interaction regulates Rho GTPase crosstalk for 3D collagen migration. Nat. Cell Biol. *16*, 909–917. https://doi.org/10.1038/ncb3026.

35. Cooper, S., Sadok, A., Bousgouni, V., and Bakal, C. (2015). Apolar and polar transitions drive the conversion between amoeboid and mesenchymal shapes in melanoma cells. Mol. Biol. Cell *26*, 4163–4170. https://doi.org/10.1091/mbc.E15-06-0382.

36. Maioli, V., Chennell, G., Sparks, H., Lana, T., Kumar, S., Carling, D., Sardini, A., and Dunsby, C. (2016). Time-lapse 3-D measurements of a glucose biosensor in multicellular spheroids by light sheet fluorescence microscopy in commercial 96-well plates. Sci. Rep. *6*, 37777. https://doi.org/10.1038/srep37777.

37. Dunsby, C. (2008). Optically sectioned imaging by oblique plane microscopy. Opt Express *16*, 20306–20316. https://doi.org/10.1364/OE.16.020306.

38. De Vries, M., Dent, L., Curry, N., Rowe-Brown, L., Bousgouni, V., Tyson, A., Dunsby, C., and Bakal, C. (2023). 3D single-cell shape analysis using geometric deep learning. Preprint at bioRxiv. https://doi.org/10.1101/2022.06.17.496550.

39. Bakal, C., Aach, J., Church, G., and Perrimon, N. (2007). Quantitative Morphological Signatures Define Local Signaling Networks Regulating Cell Morphology. Science *316*, 1753–1756. https://doi.org/10.1126/science.1140324.

40. Baker, E.L., Srivastava, J., Yu, D., Bonnecaze, R.T., and Zaman, M.H. (2011). Cancer Cell Migration: Integrated Roles of Matrix Mechanics and Transforming Potential. PLoS One *6*, e20355. https://doi.org/10.1371/journal.pone.0020355.

41. Joo, S., Oh, S.-H., Sittadjody, S., Opara, E.C., Jackson, J.D., Lee, S.J., Yoo, J.J., and Atala, A. (2016). The effect of collagen hydrogel on 3D culture of ovarian follicles. Biomed. Mater. *11*, 065009. https://doi.org/10.1088/1748-6041/11/6/065009.

42. Joshi, J., Mahajan, G., and Kothapalli, C.R. (2018). Three-dimensional collagenous niche and azacytidine selectively promote time-dependent cardiomyogenesis from human bone marrow-derived MSC spheroids. Biotechnol. Bioeng. *115*, 2013–2026. https://doi.org/10.1002/bit.26714.

43. McBane, J.E., Vulesevic, B., Padavan, D.T., McEwan, K.A., Korbutt, G.S., and Suuronen, E.J. (2013). Evaluation of a Collagen-Chitosan Hydrogel for Potential Use as a Pro-Angiogenic Site for Islet Transplantation. PLoS One *8*, e77538. https://doi.org/10.1371/journal.pone.0077538.

44. Buxboim, A., Rajagopal, K., Brown, A.E.X., and Discher, D.E. (2010). How deeply cells feel: methods for thin gels. J. Phys. Condens. Matter *22*, 194116. https://doi.org/10.1088/0953-8984/22/19/194116.

45. Maloney, J.M., Walton, E.B., Bruce, C.M., and Van Vliet, K.J. (2008). Influence of finite thickness and stiffness on cellular adhesion-induced deformation of compliant substrata. Phys. Rev. E Stat. Nonlin. Soft Matter Phys. *78*, 041923. https://doi.org/10.1103/PhysRevE.78.041923.

46. Sen, S., Engler, A.J., and Discher, D.E. (2009). Matrix strains induced by cells: Computing how far cells can feel. Cell. Mol. Bioeng. *2*, 39–48. https://doi.org/10.1007/s12195-009-0052-z.

47. Caswell, P.T., and Zech, T. (2018). Actin-Based Cell Protrusion in a 3D Matrix. Trends Cell Biol. *28*, 823–834. https://doi.org/10.1016/j.tcb.2018.06.003.

48. Bodor, D.L., Pönisch, W., Endres, R.G., and Paluch, E.K. (2020). Of Cell Shapes and Motion: The Physical Basis of Animal Cell Migration. Dev. Cell *52*, 550–562. https://doi.org/10.1016/j.devcel.2020.02.013.

49. Bravo-Cordero, J.J., Hodgson, L., and Condeelis, J. (2012). Directed cell invasion and migration during metastasis. Curr. Opin. Cell Biol. *24*, 277–283. https://doi.org/10.1016/j.ceb.2011.12.004.

50. Eddy, R.J., Weidmann, M.D., Sharma, V.P., and Condeelis, J.S. (2017). Tumor Cell Invadopodia: Invasive Protrusions that Orchestrate Metastasis. Trends Cell Biol. *27*, 595–607. https://doi.org/10.1016/j.tcb.2017.03.003.

51. Buxboim, A., Ivanovska, I.L., and Discher, D.E. (2010). Matrix elasticity, cytoskeletal forces and physics of the nucleus: how deeply do cells 'feel' outside and in? J. Cell Sci. *123*, 297–308. https://doi.org/10.1242/jcs.041186.

52. Rudnicki, M.S., Cirka, H.A., Aghvami, M., Sander, E.A., Wen, Q., and Billiar, K.L. (2013). Nonlinear Strain Stiffening Is Not Sufficient to Explain How

Far Cells Can Feel on Fibrous Protein Gels. Biophys. J. *105*, 11–20. https://doi.org/10.1016/j.bpj.2013.05.032.

53. Mullen, C.A., Vaughan, T.J., Billiar, K.L., and McNamara, L.M. (2015). The Effect of Substrate Stiffness, Thickness, and Cross-Linking Density on Osteogenic Cell Behavior. Biophys. J. *108*, 1604–1612. https://doi.org/10.1016/j.bpj.2015.02.022.

54. Hetrick, B., Han, M.S., Helgeson, L.A., and Nolen, B.J. (2013). Small Molecules CK-666 and CK-869 Inhibit Actin-Related Protein 2/3 Complex by Blocking an Activating Conformational Change. Chem. Biol. *20*, 701–712. https://doi.org/10.1016/j.chembiol.2013.03.019.

55. Nolen, B.J., Tomasevic, N., Russell, A., Pierce, D.W., Jia, Z., McCormick, C.D., Hartman, J., Sakowicz, R., and Pollard, T.D. (2009). Characterization of two classes of small molecule inhibitors of Arp2/3 complex. Nature *460*, 1031–1034. https://doi.org/10.1038/nature08231.

56. Straight, A.F., Cheung, A., Limouze, J., Chen, I., Westwood, N.J., Sellers, J.R., and Mitchison, T.J. (2003). Dissecting temporal and spatial control of cytokinesis with a myosin II Inhibitor. Science *299*, 1743–1747. https://doi.org/10.1126/science.1081412.

57. Ikenoya, M., Hidaka, H., Hosoya, T., Suzuki, M., Yamamoto, N., and Sasaki, Y. (2002). Inhibition of rho-kinase-induced myristoylated alanine-rich C kinase substrate (MARCKS) phosphorylation in human neuronal cells by H-1152, a novel and specific Rho-kinase inhibitor. J. Neurochem. *81*, 9–16. https://doi.org/10.1046/j.1471-4159.2002.00801.x.

58. Sasaki, Y., Suzuki, M., and Hidaka, H. (2002). The novel and specific Rho-kinase inhibitor (S)-(+)-2-methyl-1-[(4-methyl-5-isoquinoline)sulfonyl]-homopiperazine as a probing molecule for Rho-kinase-involved pathway. Pharmacol. Ther. *93*, 225–232. https://doi.org/10.1016/s0163-7258(02)00191-2.

59. Tamura, M., Nakao, H., Yoshizaki, H., Shiratsuchi, M., Shigyo, H., Yamada, H., Ozawa, T., Totsuka, J., and Hidaka, H. (2005). Development of specific Rho-kinase inhibitors and their clinical application. Biochim. Biophys. Acta *1754*, 245–252. https://doi.org/10.1016/j.bbapap.2005.06.015.

60. Jordan, M.A., Thrower, D., and Wilson, L. (1992). Effects of vinblastine, podophyllotoxin and nocodazole on mitotic spindles : Implications for the role of microtubule dynamics in mitosis. J. Cell Sci. *102*, 401–416. https://doi.org/10.1242/jcs.102.3.401.

61. Zieve, G.W., Turnbull, D., Mullins, J.M., and McIntosh, J.R. (1980). Production of large numbers of mitotic mammalian cells by use of the reversible microtubule inhibitor Nocodazole: Nocodazole accumulated mitotic cells. Exp. Cell Res. *126*, 397–405. https://doi.org/10.1016/0014-4827(80)90279-7.

62. Bousgouni, V., Inge, O., Robertson, D., Jones, I., Clatworthy, I., and Bakal, C. (2022). ARHGEF9 regulates melanoma morphogenesis in environments with diverse geometry and elasticity by promoting filopodial-driven adhesion. iScience *25*, 104795. https://doi.org/10.1016/j.isci.2022.104795.

63. Bousgouni, V., and Bakal, C. (2023). Quantitative imaging of single-cell phenotypes in cancer cells cultured on hydrogel surfaces. STAR Protoc. *4*, 101942. https://doi.org/10.1016/j.xpro.2022.101942.

64. Stojic, L., Lun, A.T.L., Mascalchi, P., Ernst, C., Redmond, A.M., Mangei, J., Barr, A.R., Bousgouni, V., Bakal, C., Marioni, J.C., et al. (2020). A high-content RNAi screen reveals multiple roles for long noncoding RNAs in cell division. Nat. Commun. *11*, 1851. https://doi.org/10.1038/s41467-020-14978-7.

65. Pascual-Vargas, P., Cooper, S., Sero, J., Bousgouni, V., Arias-Garcia, M., and Bakal, C. (2017). RNAi screens for Rho GTPase regulators of cell shape and YAP/TAZ localisation in triple negative breast cancer. Sci. Data *4*, 170018. https://doi.org/10.1038/sdata.2017.18.

66. Su, K.-C., Takaki, T., and Petronczki, M. (2011). Targeting of the RhoGEF Ect2 to the equatorial membrane controls cleavage furrow formation during cytokinesis. Dev. Cell *21*, 1104–1115. https://doi.org/10.1016/j.devcel.2011.11.003.

67. Charras, G.t. (2008). A short history of blebbing. J. Microsc. *231*, 466–478. https://doi.org/10.1111/j.1365-2818.2008.02059.x.

68. Bi, D., Lopez, J.H., Schwarz, J.M., and Manning, M.L. (2015). A density-independent rigidity transition in biological tissues. Nat. Phys. *11*, 1074–1079. https://doi.org/10.1038/nphys3471.

69. Devany, J., Sussman, D.M., Yamamoto, T., Manning, M.L., and Gardel, M.L. (2021). Cell cycle-dependent active stress drives epithelia remodeling. Proc. Natl. Acad. Sci. USA *118*, e1917853118. https://doi.org/10.1073/pnas.1917853118.

70. Yang, X., Bi, D., Czajkowski, M., Merkel, M., Manning, M.L., and Marchetti, M.C. (2017). Correlating cell shape and cellular stress in motile confluent tissues. Proc. Natl. Acad. Sci. USA *114*, 12663–12668. https://doi.org/10.1073/pnas.1705921114.

71. Woroniuk, A., Porter, A., White, G., Newman, D.T., Diamantopoulou, Z., Waring, T., Rooney, C., Strathdee, D., Marston, D.J., Hahn, K.M., et al. (2018). STEF/TIAM2-mediated Rac1 activity at the nuclear envelope regulates the perinuclear actin cap. Nat. Commun. *9*, 2124. https://doi.org/10.1038/s41467-018-04404-4.

72. Leong, W.S., Tay, C.Y., Yu, H., Li, A., Wu, S.C., Duc, D.-H., Lim, C.T., and Tan, L.P. (2010). Thickness sensing of hMSCs on collagen gel directs stem cell fate. Biochem. Biophys. Res. Commun. *401*, 287–292. https://doi.org/10.1016/j.bbrc.2010.09.052.

73. Dalby, M.J., Riehle, M.O., Yarwood, S.J., Wilkinson, C.D.W., and Curtis, A.S.G. (2003). Nucleus alignment and cell signaling in fibroblasts: response to a micro-grooved topography. Exp. Cell Res. *284*, 274–282. https://doi.org/10.1016/s0014-4827(02)00053-8.

74. Isermann, P., and Lammerding, J. (2013). Nuclear Mechanics and Mechanotransduction in Health and Disease. Curr. Biol. *23*, R1113–R1121. https://doi.org/10.1016/j.cub.2013.11.009.

75. Cooke, M., Kreider-Letterman, G., Baker, M.J., Zhang, S., Sullivan, N.T., Eruslanov, E., Abba, M.C., Goicoechea, S.M., García-Mata, R., and Kazanietz, M.G. (2021). FARP1, ARHGEF39, and TIAM2 are essential receptor tyrosine kinase effectors for Rac1-dependent cell motility in human lung adenocarcinoma. Cell Rep. *37*, 109905. https://doi.org/10.1016/j.celrep.2021.109905.

76. Maltas, J., Reed, H., Porter, A., and Malliri, A. (2020). Mechanisms and consequences of dysregulation of the Tiam family of Rac activators in disease. Biochem. Soc. Trans. *48*, 2703–2719. https://doi.org/10.1042/BST20200481.

77. Eden, S., Rohatgi, R., Podtelejnikov, A.V., Mann, M., and Kirschner, M.W. (2002). Mechanism of regulation of WAVE1-induced actin nucleation by Rac1 and Nck. Nature *418*, 790–793. https://doi.org/10.1038/nature00859.

78. Nakayama, M., Goto, T.M., Sugimoto, M., Nishimura, T., Shinagawa, T., Ohno, S., Amano, M., and Kaibuchi, K. (2008). Rho-Kinase Phosphorylates PAR-3 and Disrupts PAR Complex Formation. Dev. Cell *14*, 205–215. https://doi.org/10.1016/j.devcel.2007.11.021.

79. Sadok, A., and Marshall, C.J. (2014). Rho GTPases. Small GTPases *5*, e29710. https://doi.org/10.4161/sgtp.29710.

80. Sailem, H., Bousgouni, V., Cooper, S., and Bakal, C. (2014). Cross-talk between Rho and Rac GTPases drives deterministic exploration of cellular shape space and morphological heterogeneity. Open Biol. *4*, 130132. https://doi.org/10.1098/rsob.130132.

81. Xu, J., Wang, F., Van Keymeulen, A., Herzmark, P., Straight, A., Kelly, K., Takuwa, Y., Sugimoto, N., Mitchison, T., and Bourne, H.R. (2003). Divergent Signals and Cytoskeletal Assemblies Regulate Self-Organizing Polarity in Neutrophils. Cell *114*, 201–214. https://doi.org/10.1016/S0092-8674(03)00555-5.

82. Gaitanos, T.N., Koerner, J., and Klein, R. (2016). Tiam–Rac signaling mediates trans-endocytosis of ephrin receptor EphB2 and is important for cell repulsion. J. Cell Biol. *214*, 735–752. https://doi.org/10.1083/jcb.201512010.

83. Rooney, C., White, G., Nazgiewicz, A., Woodcock, S.A., Anderson, K.I., Ballestrem, C., and Malliri, A. (2010). The Rac activator STEF (Tiam2) regulates cell migration by microtubule-mediated focal adhesion disassembly. EMBO Rep. *11*, 292–298. https://doi.org/10.1038/embor.2010.10.

84. Cooke, M. (2021). Novel insights into the RTK-dependent metastatic phenotype of KRAS-mutant lung adenocarcinoma. Mol. Cell. Oncol. *8*, 2013723. https://doi.org/10.1080/23723556.2021.2013723.

85. Zhuang, B., Su, Y.S., and Sockanathan, S. (2009). FARP1 promotes the dendritic growth of spinal motor neuron subtypes through transmembrane Semaphorin6A and PlexinA4 signaling. Neuron *61*, 359–372. https://doi.org/10.1016/j.neuron.2008.12.022.

86. Cheadle, L., and Biederer, T. (2014). Activity-Dependent Regulation of Dendritic Complexity by Semaphorin 3A through Farp1. J. Neurosci. *34*, 7999–8009. https://doi.org/10.1523/JNEUROSCI.3950-13.2014.

87. Cheadle, L., and Biederer, T. (2012). The novel synaptogenic protein Farp1 links postsynaptic cytoskeletal dynamics and transsynaptic organization. J. Cell Biol. *199*, 985–1001. https://doi.org/10.1083/jcb.201205041.

88. Cooke, M., Zhang, S., Cornejo Maciel, F., and Kazanietz, M.G. (2023). Gi/o GPCRs drive the formation of actin-rich tunneling nanotubes in cancer cells via a Gβγ/PKCα/FARP1/Cdc42 axis. J. Biol. Chem. *299*, 104983. https://doi.org/10.1016/j.jbc.2023.104983.

89. Amado-Azevedo, J., Reinhard, N.R., van Bezu, J., de Menezes, R.X., van Beusechem, V.W., van Nieuw Amerongen, G.P., van Hinsbergh, V.W.M., and Hordijk, P.L. (2017). A CDC42-centered signaling unit is a dominant positive regulator of endothelial integrity. Sci. Rep. *7*, 10132. https://doi.org/10.1038/s41598-017-10392-0.

90. Hirano, T., Shinsato, Y., Tanabe, K., Higa, N., Kamil, M., Kawahara, K., Yamamoto, M., Minami, K., Shimokawa, M., Arigami, T., et al. (2020). FARP1 boosts CDC42 activity from integrin αvβ5 signaling and correlates with poor prognosis of advanced gastric cancer. Oncogenesis *9*, 1–14. https://doi.org/10.1038/s41389-020-0190-7.

91. Rafiq, N.B.M., Nishimura, Y., Plotnikov, S.V., Thiagarajan, V., Zhang, Z., Shi, S., Natarajan, M., Viasnoff, V., Kanchanawong, P., Jones, G.E., and Bershadsky, A.D. (2019). A mechano-signalling network linking microtubules, myosin IIA filaments and integrin-based adhesions. Nat. Mater. *18*, 638–649. https://doi.org/10.1038/s41563-019-0371-y.

92. Even-Ram, S., Doyle, A.D., Conti, M.A., Matsumoto, K., Adelstein, R.S., and Yamada, K.M. (2007). Myosin IIA regulates cell motility and actomyosin-microtubule crosstalk. Nat. Cell Biol. *9*, 299–309. https://doi.org/10.1038/ncb1540.

93. Botcherby, E.J., Juskaitis, R., Booth, M.J., and Wilson, T. (2007). Aberration-free optical refocusing in high numerical aperture microscopy. Opt. Lett. *32*, 2007–2009. https://doi.org/10.1364/OL.32.002007.

94. Maioli, V.A. (2016). High-speed 3-D fluorescence imaging by oblique plane microscopy: multi-well plate-reader development, biological applications and image analysis. https://doi.org/10.25560/68022.

95. Sikkel, M.B., Kumar, S., Maioli, V., Rowlands, C., Gordon, F., Harding, S.E., Lyon, A.R., MacLeod, K.T., and Dunsby, C. (2016). High speed sCMOS-based oblique plane microscopy applied to the study of calcium dynamics in cardiac myocytes. J. Biophotonics *9*, 311–323. https://doi.org/10.1002/jbio.201500193.

96. Schindelin, J., Arganda-Carreras, I., Frise, E., Kaynig, V., Longair, M., Pietzsch, T., Preibisch, S., Rueden, C., Saalfeld, S., Schmid, B., et al. (2012). Fiji: an open-source platform for biological-image analysis. Nat. Methods *9*, 676–682. https://doi.org/10.1038/nmeth.2019.

STAR★METHODS

KEY RESOURCES TABLE

REAGENT or RESOURCE	SOURCE	IDENTIFIER
Antibodies		
Tubulin Alpha antibody | YOL1/34 (Rat)	Bio-Rad	Cat# MCA78G; RRID: AB_325005
Cleaved Caspase-3 (Asp175) Antibody (Rabbit)	Cell Signalling	Cat# 9661; RRID: AB_2341188
Phospho-Myosin Light Chain 2 Antibody (Rabbit)	Cell Signalling	Cat# 3671; RRID: AB_330248
Goat anti-Rat IgM Secondary Antibody, Alexa Fluor™ 647	Invitrogen	Cat# A-21248; RRID: AB_2535816
Goat anti-Rabbit IgG Secondary Antibody, Alexa Fluor™ 488	Invitrogen	Cat# A-11034; RRID: AB_2576217
Goat anti-Rabbit IgG Secondary Antibody, Alexa Fluor™ 568	Invitrogen	Cat# A-11011; RRID: AB_143157
Chemicals, peptides, and recombinant proteins		
Alexa Fluor™ 568 Phalloidin	Invitrogen	A12380
Alexa Fluor™ 488 Phalloidin	Invitrogen	A12379
Rat Tail Type-1 collagen	Corning	354236
Penicillin-Streptomycin	Gibco	Cat# 15140122
Blebbistatin	Sigma-Aldrich	Cat# B0560
Lipofectamine™ RNAiMAX Transfection Reagent	Invitrogen	Cat# 13778075
Formaldehyde (w/v), Methanol-free	Thermo Scientific	Cat# 28908
Critical commercial assays		
96 well plate with range stiffness (Softwell 96 Glass HTS)	Matrigen	SW96G-HTS-COL
Rneasy mini Kit	QIAGEN	Cat# 74104
ABI High-capacity RNA-to-cDNA	Applied Biosystems	Cat# 4387406
SYBR™ Green PCR Master Mix	Applied Biosystems	4309155
Experimental models: Cell lines		
WM266-4 human melanoma	Marshall Laboratory, Institute of Cancer Research	RRID: CVCL_2765
A375 human melanoma	Harrington Laboratory, Intsitute of Cancer Research	RRID: CVCL_0132
WM266-4 EGFP-CAAX	Marshall Laboratory, Institute of Cancer Research	N/A
Oligonucleotides		
Oligonucleotide information including siRNA and RT-qPCR primer pairs.	See Table S6	N/A
Recombinant DNA		
YFP-TIAM2 (Species: Mouse)	Müller et al.[30]	Citrine ID: V4583
YFP-FARP1 (Species: Human)	Müller et al.[30]	Citrine ID: JB132
pcDNA3.1-eGFP	Niedzwiedz Laboratory, ICR	N/A
Software and algorithms		
Fiji image processing package	https://imagej.net/software/fiji/	N/A
MATLAB	mathworks	N/A
Python 3	http://www.python.org	N/A
R: A Language and Environment for Statistical Computing	https://www.R-project.org/	N/A
Harmony	PerkinElmer / Revvity	Harmony 5.1

(*Continued on next page*)

Continued

REAGENT or RESOURCE	SOURCE	IDENTIFIER
Other		
ViewPlate-96 Black, Glass Bottom, Tissue Culture Treated, Sterile	Revvity	6005430
PhenoPlate 96-well, black, optically clear flat-bottom, tissue-culture treated	Revvity	6055300
PhenoPlate 384-well, black, optically clear flat-bottom, tissue-culture treated	Revvity	6057302

RESOURCE AVAILABILITY

Lead contact

Further information and requests for resources and reagents should be directed to and will be fulfilled by the lead contact, Chris Bakal (chris.bakal@icr.ac.uk).

Materials availability

This study did not generate new unique reagents. The constructs introduced into cell lines are detailed in the Key resources table.

Data and code availability

- Dataset of cells in collagen on plastic substrate, are related to De Vries et al.[38], and data of shape measurements from preliminary genetic screens are related to Bousgouni et al.[62] ssOPM and other data reported in this paper will be shared by the lead contact upon request.
- This paper does not report original code.
- Additional information required to reanalyse the data reported in this paper is available from the lead contact upon request.

EXPERIMENTAL MODEL AND STUDY PARTICIPANT DETAILS

WM226-4 (RRID:CVCL_2765) and A375 (RRID:CVCL_0132) cell lines are each derived from female patients. Cells were maintained in Dulbecco's Modified Eagle Medium (DMEM), with 1 percent penicillin-streptomycin (Thermo Fisher) and 10 percent Fetal Bovine Serum (FBS) (ThermoFischer). Cells in culture were maintained at 5 percent CO2 in a humidified incubator at 37° Celsius. Cells were passaged using 0.25 percent Trypsin-EDTA (Thermo Fisher). Cell lines were confirmed to be mycoplasma negative (e-Myco plus Mycoplasma PCR detection kit, iNTRON Biotechnology, and MycoStrip™ - Mycoplasma Detection Kit, InvivoGen).

METHOD DETAILS

Cell culture

WM266-4 melanoma cells expressing CAAX-GFP (donated by the Marshall lab) and A375 cells, were grown in Dulbecco's Modified Eagle Medium (DMEM) supplemented with 10% heat-inactivated bovine serum (FBS) and 1% penicillin/streptomycin in T75 flasks. Cells were cultured at 37°C and supplemented with 5% CO_2 in humidified incubators. WM266-4 and A375 melanoma cells tested negative for mycoplasma (e-Myco plus Mycoplasma PCR detection kit, iNTRON Biotechnology, and Myco-Strip -Mycoplasma Detection Kit, InvivoGen).

Cell preparation for imaging, siRNA and inhibitor treatments

WM266-4 cells imaged in collagen hydrogels in glass 96 well plates were prepared as follows. WM266-4 melanoma cells expressing CAAX-GFP were reverse transfected with OnTARGETplus SMARTpool (Table S6), at stock concentration 20 μM in 6 well plates. For ssOPM siRNA experiments the CONTROL treatment is mock transfection with transfection reagents but no siRNA. Transfections were carried out using Lipofectamine RNAimax (Invitrogen) according to the manufacturer's instructions. On the second day after transfection, 10^5 cells/ml were re-suspended in 500 μl of 2.3 mg/mL collagen rat tail (Gibco). A 100 μl volume of the collagen and cell mixture was dispensed in quadruplicate wells onto poly-D-Lysine (0.1mg/ml) coated glass bottom view 96 well plates (PerkinElmer). Plates were centrifuged @1200 rpm for 5 minutes at 4°C and incubated overnight in a tissue culture incubator. After incubation, cells were fixed with 4% methanol free PFA for 30 mins at RT. Wells were stained with DRAQ5 at a concentration of 5 μM, to label nuclei. siRNA treatments for WM266-4 or A375 for 2D confocal imaging or qPCR were prepared in 6 well plates following the same siRNA protocol, and either transferred to imaging plates or prepared for qPCR on the second day after transfection. All small molecule inhibitor treatments were 6 hours, unless indicated otherwise. Blebbistatin treatments in experiments with siRNA against *FARP1* or *TIAM2* were 25 μM unless indicated otherwise. Treatments for collagen hydrogels on plastic are from the De Vries et al.

dataset and were prepared in similar collagen conditions to those described above with a target final collagen concentration of ~2 mg/mL, and are detailed in De Vries et al.[38] Treatments for this dataset were: Blebbistatin (10 μM), H1152 (10 μM), CK666 (100 μM), Nocodazole (1 μM), and DMSO 1 in 1000. These concentrations were calculated including the 100 μl volume of the collagen hydrogel.

Stage-scanning oblique plane microscopy (ssOPM) setup

Oblique plane microscopy was performed using a setup reported previously[36] and a schematic is shown (Figure S7A). For collagen hydrogels on glass 96 well plates (i.e., excluding ssOPM data for Figures 1G and 2, which are collagen on plastic), the imaging system including, microscope setup, acquisition, reslicing and segmentation and shape measurements are described below. For data from collagen hydrogels on plastic coverslips (e.g., Figures 1G and 2) a similar but modified version of the imaging system was used. A key change in the imaging system in the collagen on plastic dataset, was that each colour channel was detected sequentially and no image registration was required. This is because the system returned to the same location rapidly enough to avoid drift. A full description of modifications are detailed in De Vries et al. [38]

Five excitation sources at different wavelengths (457, 488, 515, 561, 642 nm) are combined onto a common optical path using dichroic mirrors. An acousto-optic tunable filter – allowing switching and power control – is used to selectively couple the beams into a single-mode polarisation-maintaining fibre.

Light exiting the fibre is collimated (L1) then focused in the horizontal direction by a cylindrical lens (C1) onto the back focal plane of spherical lens L2. This results in a vertically orientated light sheet at 55 degrees to the optical axis of O2. The microscope formed by O2 and TL2 relays the light sheet to the image plane of the camera port of a commercially available microscope frame (Olympus IX71). The commercial microscope (comprising TL1 and O1) relays the light sheet to the image plane of O1. O1 is a 60X/1.2NA water immersion objective (Olympus UPLSAPO60XW). The microscope objective was fitted with a collar to provide a continuous supply of water immersion liquid.

The overall magnification between the image planes of O1 and O2 is set to be equal to the ratio of the refractive indices for the images formed at O1 (water) and O2 (air) to ensure that the lateral and axial magnification between the focal planes of O1 and O2 are equal.[93] The excitation light sheet produced across the focal plane of O1 excites fluorescence from the sample. The resulting fluorescence image is relayed back to the focal plane of O2. O3 is positioned at 35 degrees to the optical axes of O1 and O2, such that the fluorescence image of the region illuminated by the light sheet in the sample is perpendicular to its optical axis, and conjugate with the focal plane of O3. Together with tube lenses TL3a and TL3b, this system relays an image of the fluorescence emitted within the light sheet to the two sCMOS cameras. A dichroic beam splitter (DC) and emission filters (EM1, EM2) separate emitted fluorescence for two-colour imaging.

ssOPM image acquisition

Stage-scanning OPM was implemented in a similar way to Maioli et al.[36] In, brief a motorised stage (SCAN-IM 120 × 80, Marzhäuser) controlled by a driver unit (Tango 2 fitted with AUX I/O option, Marzhäuser) outputs a TTL trigger each time it has travelled a predefined distance (1.4 μm for the results presented here). The TTL output is connected to a digital acquisition box (DAQ) (National Instruments NI USB-6229) configured to output a pattern of signals each time a TTL signal is received from the x-y stage. The signals control the laser power and illumination duration, and trigger the start of camera exposures. The stage scans in the y direction, as shown (Figure S7A). During acquisition a scan speed of 0.1 μm ms^{-1} was used. A speed of 10 μm ms^{-1} was used to move between wells.

The two sCMOS cameras (PCO.edge, PCO) were both operated in Global Reset acquisition mode with 1280x1000 pixels. The exposure time was defined by the 2 ms laser exposure time. The two spectral channels were interleaved temporally to prevent cross-talk between channels. Per field of view, the x-y stage was scanned 4200 μm in the y direction (corresponding to 3000 frames per camera). Each field of view corresponded to 7.32 GB of data per channel and took 42 s to acquire. Image acquisition was controlled by a HP z840 PC with 128 GB of RAM and a 4x1 TB SSD configured in RAID 0. Saving and moving to the next well took a further 66 s (for a total of 108 seconds per well).

Volumetric imaging in 3 spectral channels (2× fluorescence and 1× scatter) was performed in two stages. The first stage acquired the two fluorescence spectral channels (CAAX-GFP and DRAQ5) for the entire plate. In the second stage, the image acquisition was repeated but now with scattered light from collagen imaged on camera 1 with 488 nm excitation and in the absence of an emission filter. Camera 2 was used to image the DRAQ5 channel for a second time. As images of DRAQ5 were acquired in both stages, they could then be used to measure any drift between image sets and thus enable the two sets to be co-registered.

ssOPM image reslicing and registration

The average background level was measured for each camera by taking the average pixel value over a field of view acquired with no laser on. This was subtracted from the data prior to reslicing.

The 2D transform to co-register camera 1 and camera 2 was measured based on a 2-channel fluorescence image acquisition of a sample of 100 nm four-colour fluorescent beads (TetraSpeck, Thermofisher) in 10% agarose. The x-y shift, magnification and rotation

needed to co-register the data acquired on camera 2 to that of camera 1 was measured manually using a custom script in MATLAB (imtranslate, imrotate, imscale and fliplr: Image Processing Toolbox, MATLAB). This transform was applied to all raw image data acquired on camera 2 prior to reslicing.

Raw ssOPM images are a set of image planes at 55 degrees to the optical axis of O1. The data was transformed into conventional coordinates (z parallel to the optical axis, x&y&z perpendicular). Reslicing was performed using a bi-linear interpolation algorithm.[94] To increase speed, a custom-written Java implementation of the algorithm was used. For all image segmentation and cell shape analysis, raw camera images were binned by factor of 4 - prior to reslicing - to reduce data volume and analysis times. Images presented in figures in this paper were resliced with factor 2 binning. After reslicing voxel sizes were 1x1x1 m^3 (for analysis) and 0.5x0.5x0.5 m^3 (for display).

The collagen channel was coregistered in 3D with the fluorescence channels using the imregtform (Image Processing Toolbox, MATLAB) using the default optimizer parameters. The transform was measured on the DRAQ5 channel, which was common to both acquisitions, and applied to the collagen channel using the 'imwarp' function in MATLAB.

ssOPM image segmentation

Prior to segmentation, the collagen channel was viewed manually. Any volumes where the collagen was not present throughout the entire volume were rejected from analysis.

To verify the robustness of the 3D segmentation used in this paper, two methods were tested. An intensity-threshold-based approach using an Otsu threshold and an active contour method, which uses energy minimisation (Figure S7B). Both methods generate a mask with minimal user input so can be applied to large datasets. For both methods, cells and nuclei were segmented in 3D.

Prior to segmentation, the tips of the parallelepiped-shaped volume imaged by the ssOPM image acquisition were removed by cropping in the y direction. This removed any parts of the volume which were not imaged over its full axial extent due to the light-sheet angle.

In the intensity-based method, thresholds were measured automatically for each field of view. The nucleus threshold was selected using Otsu's method with a single level (multithresh, Image Processing Toolbox, MATLAB). The cell body was masked using a similar method. In this case there were 3 intensity levels in the image, background, brightly fluorescent cell membrane and dim fluorescent protrusions. To include all parts of the cell in the final mask, the lowest threshold found by a two-level Otsu method was used.

In the active contour method, an initial guess of the mask was generated using a threshold of 5 digital numbers (just above the background). The final mask was formed after 500 iterations (nuclei) or 1000 iterations (cell) of the active contour method (Image Processing Toolbox, MATLAB).

The final nucleus mask was generated for both methods by separating touching nuclei. To achieve this, the Euclidean distance transform (bwdist, Image Processing Toolbox, MATLAB) was used on the inverse of the mask to determine the distance of each voxel to the edge of the 3D mask. A watershed (Image Processing Toolbox, MATLAB) was used on the negative of the distance transformed image to separate nuclei based on regions where the mask narrows. Nuclei with volume less than 250 μm^3 were rejected at this stage.

As the nuclei are part of the cell, an OR operation is applied to the cell mask and the nucleus mask to generate a combined mask. Any connected components in the cell binary mask which do not contain a nucleus were rejected. Touching cells are separated using a marker-based watershed approach. Nuclei are set as the low points (digital value 0), the cell body (digital value 1) as intermediate points and the background as high points (digital value infinity). The watershed finds the halfway point between touching nuclei. The watershed then underwent an AND operation with the original cell mask to generate a final mask. Following segmentation, cells touching the edges of the image volume are removed. Cells with volume below 512 μm^3 were rejected. Nuclei of rejected cells were removed from the nucleus mask.

ssOPM image measures

Cell and nucleus shape measures were read out using the regionprops3 (Image Processing Toolbox, MATLAB). Further statistics were derived from the outputs of this function as described in (Table S1 and Table S2).

Confirmation that shape changes between environments are robust to segmentation method and ssOPM light sheet PSF shape

Segmentation method

We test two methods for unsupervised segmentation of a full 3D dataset of cells. We tested, on control cells, a method which segments based on an Otsu threshold set for each field of view and an active contour method (both segmentation modes are described in detail in the STAR Methods section). We show the features measured using both segmentation methods (Figure S7B). They are separated into coverslip proximal and distal groups based upon nucleus position with respect to the coverslip (as outlined in the previous section). For most of the features the Otsu and active contours methods give similar values. Changes between coverslip proximal and distal cells appeared consistent between threshold and active contour based segmentation. Overall this suggests that results are repeatable between segmentation methods. As either segmentation method is viable for this dataset, the Otsu threshold approach was chosen due to the shorter computation time.

Anisotropic PSF shape

In light-sheet microscopy, the point spread function (PSF) is usually not spherical. The FWHM spatial resolution of this ssOPM system has been previously reported as 0.5 μm in the plane of the light sheet, with a light sheet thickness of 3.8 μm at the waist. The light thickness increases to 5.4 μm over a distance of 50 μm from the centre of the field of view.[95] We set out to establish whether the anisotropic PSF might affect coverslip proximal cells - that are more likely to be flatter - differently to coverslip distal cells. We therefore eroded the cell and nucleus masks from all segmented data by an object approximating a worst-case PSF. This was performed using MATLAB's 'imerode' function with a morphological structuring element consisting of a 1x1x5 pixel kernel angled at 45° to the coverslip plane (closest possible approximation to a 55° light sheet angle). The voxel size in the image data was 1 μm^3, so this corresponds to a 1x1x5 μm^3 PSF.

Figure S7C shows pair plots of cell features for the thresholded mask (normal) and the eroded (imerode) version. Coverslip proximal and distal cells have similar normalised distributions for normal and eroded masks. This suggests that, for the selected features, the anisotropy of the mask has limited impact on the comparison between coverslip proximal and distal cells.

Spatially varying light sheet thickness

The ssOPM microscope uses an illumination light sheet with a confocal parameter of 100 μm. Therefore, the thickness of the light sheet varies as a function of the z range and is thinner at the centre of the z-range than the edges. Coverslip distal cells tend to be closer to the centre of the z range than coverslip proximal cells. Therefore cells on the coverslip experience a different PSF, which may affect the features measured.

To quantify this effect a reference sample of cells plated on the coverslip (no collagen) was used (referred to as the test plate). The same cells were imaged at three different z positions corresponding to the top, middle and bottom of the axial range. Example images are shown in Figure S7D. Cells from the test plate and collagen assay were grouped into bins (bottom, middle and top) based on their z coordinate (0-48, 48-96, 96-144 μm). Values were then normalised to the mean value for that feature in the lowest (first) bin.

Figure S7E shows side by side plots of the features from the test plate and control cells from the collagen plates. Feature values were normalised by dividing by the average value in the bottom bin. On the test plate, cell surface area and the angle between cell and nucleus are both within one standard deviation of one at all heights, suggesting they are not significantly changed by the spatially varying PSF. Cell protrusivity increases in the middle bin of the test plate but a decrease in protrusivity is observed in the same bin on the collagen plate. This suggests that the decrease in protrusivity observed in coverslip distal cells is due to the change in physical environment and not due to the light sheet thickness. Nucleus minor axis shows a decrease below 1 in both the middle and top bins, however this decrease is not seen in the collagen plate. Cell and nucleus volume were also tested for the test plate, but this metric was found to be affected by the spatially varying light sheet thickness. This is expected for the thin flat cells used in the test plate, which represent a deliberate worst case, as these cells are generally thinner than the light-sheet thickness. The cell volume metric was therefore not used in the analysis in this paper. We concluded that the behaviours of 'cell surface area', 'angle between', 'protrusivity' and 'nucleus minor axis' in the collagen plate are not explainable by the PSF shape alone and are dominated by other factors.

Measuring 3D collagen environment by scattered light intensity

We considered the possibility of compaction of collagen by centrifugation, deposition or by cells. We use scattered light intensity from collagen to look at whether there were gradients or differences in the local density and structure of collagen, between cell-dense proximal regions and less cellularized distal regions (Figure S1).

ssOPM data processing

Segmentation quality control

For data from collagen hydrogels on glass coverslip, we aimed to remove cells and nuclei that could not be segmented accurately due to low levels of CAAX-GFP signal, as well as cells with surface areas that are conspicuously large due to under-segmentation. To remove cells that were improperly segmented due to low expression of the *CAAX-GFP* transgene, we removed cells that had both: (i) low CAAX-GFP intensity (an average intensity of less than 1000 in camera digital numbers); and (ii) a nuclear-to-cell volume ratio of greater than 0.95. These cells were removed from subsequent analysis as they represent nuclei with cells that cannot be appropriately measured due to low CAAX-GFP signal intensity. We also aimed to remove incorrectly segmented cells with aberrant surface area (more than ~7.3 standard deviations above the mean). Applying these criteria removed approximately 350 cells (~ 1.2 % of the original total).

To remove improperly segmented cells from the collagen on plastic dataset, we processed all treatments of interest uniformly by eliminating cells that were too dim for shape analysis due to having a measurement of less than 70 mean CAAX-GFP intensity, or a measurement of less than 5 mean nucleus intensity (~ 10.21 % of the original total). We also aimed to remove incorrectly segmented cells by eliminating cells with nuclear-to-cell volume ratio greater than 0.95 (additional 0.27 %), and with aberrant surface area (approximately 1.4 standard deviations below or 5.2 standard deviations above the mean), or nucleus volume (approximately 5.6 standard deviations above the mean), which removed a further ~ 0.67 % of cells. In total, quality control for treatments of interest in the collagen on plastic dataset reduced the original ~41,955 observations to 37,276.

Coverslip localisation

The position of the coverslip was estimated using the fluorescence in the nucleus channel. To account for spatial variations in the axial position of the coverslip over the field of view, the nucleus channel was divided into 16 segments in the y direction and the average signal in each x-y plane was found for each z position in each segment. For each segment, the coverslip location was defined as the point when the signal first reaches 45% of its maximum value when moving in the positive z direction. A full 2D map of coverslip height was then produced from the 16 measurements using bilinear interpolation, giving a smooth change of coverslip height across the field of view. This map of coverslip height reflects the spatial variation across the field of view. However, this broad method does not account for variations in nuclear intensity between knockdowns and between plates, therefore there is a remaining global offset in coverslip position for each well that is accounted for in the next step.

Nucleus height determination

Following coverslip position estimation, we calculated the lower boundary of the mask for each nucleus above the coverslip (the bottom of the nucleus). To remove the remaining global offset in the coverslip position, we found the nucleus with the lowest calculated height in each ssOPM subvolume (one subvolume per well in collagen on glass, and three subvolumes per well in collagen on plastic dataset) and subtracted this value from the height of every nucleus so that the lowest nucleus in each subvolume had a distance above the coverslip of zero. Finally, for collagen on glass we corrected for wells where microscopic detachment of collagen (less than 6 microns) from the well bottom had occurred after fixation but before imaging. These wells were identifiable by discontinuities in nuclear height distributions between cells at the lowest position (attached to the coverslip) and a larger number of cells in the lowest extent of the collagen gel. In these cases, the lowest positioned cell in the collagen was also registered to the height of the coverslip. The median position adjustment was 1.17 micrometres.

Feature reduction and feature normalisation

For each ssOPM dataset we originally computed more than 20 measurements of cell and nuclear shape features, and subsequently reduced this set to a set of four features. For the indicated features in each ssOPM dataset, we used clustering to remove the most highly correlated features as follows. First, we used single-cell data to calculate Pearson correlation values between each feature using the 'cor()' function in R. For clustering, we transformed these coefficients into a distance metric by subtracting absolute Pearson correlation values from 1 and using the as.dist() function in the R package "stats." Absolute values were used so that features with similar magnitude of positive or negative correlation are both regarded as having similar distances, and the subtraction from 1 is intended so that a higher correlation translates to a smaller distance. The features were then hierarchically clustered using this metric with the 'hclust()' function in R, and the 'complete' linkage method. The resulting clusters were partitioned into four groups, and a single cell or nuclear feature was chosen as a representative feature for each group. Feature reduction was performed using the shape measures from cells that remained in a dataset after segmentation quality control.

To allow for comparison between plates that were prepared and imaged on different days, we normalised single-cell measurements for cell and nuclear features within each plate. We performed normalisation by dividing feature measurements for a single cell, by the plate median across all conditions for cells in that feature. Tables S3 and S4 indicate the number of cells for ssOPM treatment conditions.

Where indicated we performed alternative normalisation using *Z* score or min-max normalisation. *Z* scores were used for heatmap visualisation of ssOPM data, and for statistical tests and visualisation of 3D sphericity. For ternary plot visualisation using single cell data we performed additional outlier removal, where outliers were defined as values more than 1.5 × IQR (Inter Quartile Range) above the third quartile (Q3) or below the first quartile (Q1), followed by min-max normalisation.

ssOPM maximum intensity projections for example visualisation

Maximum intensity projections in xy, xz, and yz dimensions are used to visualise ssOPM volumes of collagen embedded cells. For the collagen on glass dataset, cells used for stacked maximum intensity protrusivity projections were pseudo-randomly selected. The projected cells were the first 'n' cells in our dataset that matched the protrusivity or other criteria. For the collagen on plastic dataset projections, images were log-transformed in Python with numpy.log, to better visualise a wide range of values.

3D renders are displayed as a 3D projection with trilinear interpolation using the Volume Viewer 2.01 Fiji plugin[96]. 3D surface renders were generated using the 3D viewer in Fiji. The same defined ssOPM datasets are analysed across multiple figures (Tables S3 and S4). Accordingly, images in different figures that are taken from subregions of the same ssOPM volumes are highlighted in figure legends where possible, and not represented as depicting separate experiments.

Bleb and elongation assay from raw ssOPM data

Non-resliced, full resolution ssOPM images of cells for control, si*FARP1*, and si*TIAM2* conditions were scored by eye for blebs or elongated protrusions with rear polarised nuclei. Scoring was blinded via a Python script to generate random filenames for each ssOPM volume. Estimates of the frequency of phenotype in a well were calculated from the number of cells with the observed phenotype, divided by the number of segmented cells in that well.

ssOPM data visualisations, stacked maximum intensity projections, heatmaps and general plotting

Heatmap visualisations were prepared using the Complex Heatmap package in R, or heatmap in base R. Heatmap colouring of scatter plots are with geom_pointdensity(), from the ggpointdensity package in R, values in Density legend range from 0 to approximately

1600. Boxplots and violin plots were generated in R using the ggplot2 package geom_boxplot(), and geom_violin(). For charts presenting individual data points and boxplot representations of the same data, we do not depict boxplot outliers as these are already indicated by the observations. Boxplot whisker lengths are generated using the default of 1.5 × the IQR. Contour lines in estimates of density for elongation versus roundness are generated from geom_density_2D(), from ggplot2, and density estimates for ternary plots used stat_density_tern() from ggtern package, with the n and bdl parameters: n = 100, and bdl = 0.01.

Plotting of preliminary screens of shape regulation

Plotting and heatmap summaries of preliminary screens are provided to describe the process of selecting genes for further study by ssOPM. The gene symbol matching for heatmaps/plotting was performed in an automated fashion. Gene names from the siOTP and siGenome libraries were matched to HGNC symbols using the multi symbol checker online application. Matching approved symbols were selected, and where no approved symbol was found, matching alias symbols that were RhoGEF/GAP/GTPases or related genes were selected. For the siOTP library where cell number information was available, siRNA treatments with cell numbers more than 1.5 standard deviations below the mean were removed from consideration so as to focus on direct effects of shape separately from effects on viability. Genetic treatments from the siGenome library were considered if they were also present in the siOTP library. For gene symbols in the siGenome library beginning with "LOC", the gene IDs were queried and assigned.

2D imaging, measurements, and assays

Confocal imaging in 2D used the Opera Phenix Plus High-Content Screening System. Imaging for morphology analysis used 20x water objective NA 1.0, and imaging to visualise subcellular localisation of GFP and YFP-tagged proteins used 63x water objective NA 1.15. Imaging plates were PerkinElmer PhenoPlates or Softwell Hydrogels. Cell shape measurements from 2D confocal images for this study were made using Harmony 5.1 software (Perkin Elmer). Cell measurements were made based on segmentation from tubulin staining. Measurements in the analysis of preliminary screens (eg. Figure S2) were generated as part of Bousgouni et al.[62], and used Columbus software (Perkin Elmer). For 2D experiments with thin collagen coating of tissue culture plates, the indicated amount of collagen was prepared in PBS and deposited on 96 well plates for 2 hours at room temperature before washing with PBS. For 2D assays, unless indicated otherwise, the thin collagen coating concentration was 10 $\mu g/cm^2$. In 2D assays measuring cell roundness, the roundness feature was selected as a 2D surrogate of 3D protrusivity because 3D sphericity was a cell shape feature that has high correlation with protrusivity. For 2D blebbistatin treatment assay, the experiment was in a 384 well plate format with collagen coating, and the combined number of single cells per treatment condition was at least 2100 for treatments involving the DMSO control, and at least 1200 for treatments involving blebbistatin. Assays of anti-Cleaved-Caspase-3 were in 384 well format. Target seeding densit in 384 well plate assays was 5×10^2 cells per well. For A375 experiments, the combined number of single cells per combination of siRNA and collagen condition was at least 3800.

Measurements for 2D substrates at a range of stiffness

For 2D experiments on collagen at a range of stiffness, siRNA treated cells were transferred to 96 well plate Softwell Hydrogels, coated with collagen I. The targeted seeding density was 2×10^3 cells per well. Cells were fixed in 4% PFA after 24 hours, stained with phalloidin and anti-Tubulin. Roundness measurements were made using the Perkin Elmer Harmony5.1 software. Due to the uneven surface of collagen coated wells, a pre-scan of the plate and Harmony analysis script was used to detect the correct imaging plane in the z-axis before final imaging. Prior to analysis quality control aimed to removed incorrectly optically sectioned and imaged wells. This removed one well out of 96, with an aberrant average cell area more than 8 standard deviations above the mean. Final data are from more than 67,000 single cells as indicated in Table S5.

FARP1 and *TIAM2*, 2D expression assay

Plasmids with cDNA encoding *FARP1* (Human) and *TIAM2* (Mouse) or GFP were transfected into WM266-4 using effectene transfection reagent. On the second day after transfection, approximately 2×10^3 cells per well were transferred to 96 well plates (Phenoplate, Perkin Elmer) for 24 hours before fixation and staining in 4 % PFA for 20 minutes at room temperature. This seeding density was selected in order to assay the shape of subconfluent cells. Thin collagen coating on tissue culture plastic was 10 $\mu g/cm^2$. Cells expressing transgenes were selected by calculating z-scores for GFP or YFP signal within each transgene treatment, then classifying cells with a z-score greater than 1.5 as expressing. For quality control of automated fluorescence-based cell detection, a fraction of observations ($\sim$ 0.52 percent) were removed in order to exclude small fluorescent particles and cell fragments that were not genuine cells. These particles were defined as objects where the area of signal in the nucleus and cell fluorescence channel were identical, as well as objects with fluorescence in the nuclear channel that had an area $\sim$2.5 standard deviations below the average nucleus area. In all treatments, cells with fluorescence expression z-score greater than 10 were excluded as outliers, to avoid measuring the deleterious effects of super-physiological transgene expression. For statistical tests in expression assays comparing shape parameter at the well level, data for each condition are from between 49,143, and 102,962 non-expressing cells, and between 687 to 1230 transgene expressing cells. Scoring the predominance of filaments, ruffles and blebs in GFP and YFP-TIAM2 expressing cells was performed manually.

Real time quantitative PCR

For real time quantitative PCR (also qPCR) experiments involving siRNA, WM266-4 cells were seeded into 6 well tissue culture plates and two wells per condition were transfected with siRNA, using the same protocol and siRNA reagents as described for 3D ssOPM experiments. Cells were harvested and RNA was extracted using RNeasy Plus Mini Kit (QIAGEN #74134). cDNA conversion was using the High-Capacity RNA-to-cDNA Kit (Catalogue Number 4387406). For the experiments described in Figures S2 and S3, qPCR reactions were measured from replicate samples (with either 3 or 4 replicates for each gene of interest), and compared to the average of *GAPDH* measurements. For the experiments measuring only *FARP1* or *TIAM2*, separate qPCR reactions were performed using 10 ng, 20 ng and 100 ng cDNA templates. qPCR reactions were each with 3 replicates for gene of interest, and for *GAPDH*. PCR reactions were performed on an Applied Biosystems® QuantStudio™ n6 Flex Real-Time PCR System, using SYBR Green PCR Master Mix (Ref#4309155). Primers were predesigned KiCqStart Primers (Sigma), and primers to the *GAPDH* gene were used for normalisation between samples. The changes in gene expression between different samples or conditions were calculated using the $2^{-\Delta\Delta C(T)}$ method.

Immunostaining and dye staining

Cells were fixed in 4% PFA at room temperature for 15-20 minutes, permeabilized with 0.2% Triton-X, and blocked in 2% BSA for an hour. Primary antibodies were applied overnight at 4°C, followed by secondary antibodies for one hour at room temperature. Phalloidin and nuclear dyes were added post-secondary staining, with three PBS washes after each step. Primary antibody concentrations were anti-Tubulin (1:1000 dilution), anti-Phospho-Myosin Light Chain 2 (1:50 dilution) and anti-Cleaved Caspase-3 (1:100 dilution).

Statistical methodology

We did not use prior tests to calculate sample size and statistical power. For 3D and 2D imaging experiments measuring morphology, we performed automated quality control of segmentation as described in each method section, and unless otherwise indicated these were performed uniformly across treatments as described in the 3D (ssOPM) and 2D imaging and data acquisition methods.

ssOPM statistical data analysis

As some of the ssOPM cell and nuclear shape features did not have a normal distribution, we used non-parametric tests, unless otherwise indicated. To test differences between two conditions, we used a paired Wilcoxon test with Benjamini-Hochberg (BH) adjustment for multiple comparisons. BH adjustments were performed using the R ggpubr package. Unless indicated otherwise, for tests of difference between more than two conditions, we used a Kruskal-Wallis test, followed by a Dunn's test, with BH adjustment, to discern which conditions differed from control. Unless stated otherwise, tests for differences in normalised shape measures between groups, were performed on summary statistics calculated for wells, from multiple experimental repeats (as indicated in the figures). Statistical tests were performed with functions in the R programming language and environment. Fligner tests were performed with the R stats package function 'fligner.test()'. Principal component analysis was performed on cell measurements aggregated at the well level, using the 'prcomp()' function in R.

W-statistic for common language effect size analysis of siRNA treatments on protrusivity

For common language effect size analysis, we used well-level median summaries and performed an exhaustive series of Wilcoxon rank-sum tests (Matlab) between the protrusivity measurements from each siRNA treatment. We then use the W-statistic (in conjunction with sample size) to calculate the ''common language effect size'' that each treatment has on protrusivity. We then created a matrix of pairwise comparisons between all of the siRNA treatments used in this study, and measured the degree of difference between median protrusivity in each of them. We then clustered treatments according to their statistically determined differences in protrusivity, which produced two distinct clusters in proximal and distal settings. These correspond to low and high protrusivity clusters. Analysis was performed in Matlab and plotted in R.

QUANTIFICATION AND STATISTICAL ANALYSIS

Statistical details of experiments such as sample numbers, measures of centre, and statistical tests can be found in figure legends. Analysis was performed in R, and Matlab. Unless stated otherwise, statistical tests for ssOPM data were performed on experimental batch normalised data (STAR Methods). Information about data quality control, and automated quantification are in Method details. Except where stated otherwise, statistical significance was defined as * = $p < 0.05$, ** = $p < 0.01$, *** = $p < 0.001$, **** = $p < 0.0001$. And non-significant test statistics were: ns = $p > 0.05$. For t-tests, we used the Shapiro-Wilk tests to check for evidence of deviation from the assumption of normality.